Transportation Research Part C 192 (2026) 105926

Contents lists available at ScienceDirect

Transportation Research Part C

journal homepage: www.elsevier.com/locate/trc

From micro to macro: Characterizing heterogeneity of mixed-autonomy traffic flow

Chenguang Zhao, Huan Yu *

Thrust of Intelligent Transportation, The Hong Kong University of Science and Technology, Guangzhou, China

A R T I C L E I N F O

Keywords:
Mixed autonomy
Traffic heterogeneity
Autonomous vehicle
Traffic flow theory

A B S T R A C T

Autonomous-vehicle (AV) driving strategies are typically designed and analyzed at the vehicle level, yet their macroscopic impact remains insufficiently understood. This challenge is particularly pronounced in mixed-autonomy traffic, where AVs and human-driven vehicles (HVs) may exhibit substantial behavioral heterogeneity both across and within vehicle classes. Meanwhile, most available AV data are Lagrangian vehicle trajectories, whereas macroscopic model validation generally requires Eulerian spatiotemporal measurements over road segments, which remain scarce for mixed-autonomy traffic. To bridge this gap, we first characterize heterogeneity through microscopic driver-behavior attributes. Experiments across multiple traffic datasets reveal that intra-class heterogeneity, within both AVs and HVs, can exceed the average inter-class differences. Motivated by this finding, we introduce a continuous-valued flow attribute into a generic second-order macroscopic traffic model that governs the conservation of both mass and traffic heterogeneity. In Lagrangian coordinates, the flow attribute characterizes the intrinsic behavior of individual vehicles, whereas in Eulerian coordinates, it represents the average behavioral attribute at a given spatiotemporal location. The resulting formulation establishes an interpretable micro-macro relation by linking differences in vehicle driving behavior to variations in macroscopic traffic characteristics, as reflected in the fundamental diagram. We then develop two reconstruction methods to infer this flow attribute from vehicle trajectories: a physics-based formulation when historical data are available and a neural-network-based method that relies only on local spatiotemporal data. Experiments validate that the proposed approach effectively captures traffic heterogeneity by separating the speed-density scatter points in the fundamental diagram into attribute-dependent groups. Compared with the Aw-Rascle-Zhang model benchmark, the proposed heterogeneity-based model reduces validation error up to 20 %. Detailed analyses further show that the model generalizes well, maintaining nearly the same accuracy when evaluated under previously unseen traffic conditions.

1. Introduction

Autonomous vehicles (AVs) have made significant advancements in real-world applications. In mixed-autonomy traffic, where traditional human-driven vehicles (HVs) share the road with AVs, many research works have focused on the role of AVs in improving traffic systems at the microscopic scale. These studies often regulate the behavior of individual vehicles or inter-vehicle dynamics to optimize traffic characteristics, such as capacity, stability (Wang et al., 2021; Shi et al., 2023; Stern et al., 2018), safety (Zhao

* Corresponding author.
E-mail address: huanyu@hkust-gz.edu.cn (H. Yu).

https://doi.org/10.1016/j.trc.2026.105926
Received 29 January 2026; Received in revised form 11 June 2026; Accepted 7 August 2026

et al., 2023, 2024), emissions (Sun et al., 2020a; Ercan et al., 2022), and efficiency (Li, 2022; Barth, 2024; Jiang et al., 2024). As the scale of the system grows from vehicle platoons to road traffic, microscopic modeling and design become computationally intensive, necessitating a shift to macroscopic models that describe the dynamics of aggregated traffic. Macroscopic traffic flow models are crucial for understanding the broader impact of AVs on mixed-autonomy systems.

1.1. Micro-to-macro flow modeling for mixed-autonomy traffic

Most research on mixed-autonomy flow modeling can be categorized into two approaches. The first approach treats traffic systems as multi-agent systems and derives a macroscopic limit as the number of agents approaches infinity, by using kinematic limits or the mean-field theory. The second approach directly adopts flow models by adjusting model parameters or dynamic formulations to account for mixed traffic conditions.

The continuum model is obtained as the kinematic limit of the vehicle particle model, in which the number of vehicles tends to infinity while the total mass is preserved (Chiarello et al., 2020; Dimarco et al., 2022). The derived model provides a rigorous formulation that reveals the microscopic mechanisms underlying the macroscopic model terms. However, the high analytical complexity of this approach has restricted the derivation of the macroscopic limit to only a few simple feedback-form AV controllers (Chiarello et al., 2021; Holden and Risebro, 2024; Tordeux et al., 2018). The mean-field game approach models each driver as an optimizing agent whose cost depends on the aggregate traffic distribution. The resulting mean-field equilibrium, at which no driver can reduce their cost by unilaterally changing their driving strategy, provides a macroscopic description of traffic dynamics (Huang et al., 2020; Li et al., 2022; Mo et al., 2024). The equilibrium is obtained by solving a coupled backward Hamilton-Jacobi-Bellman (HJB) PDE that describes the optimal actions of individual vehicles, and a forward Fokker-Planck-Kolmogorov (FPK) PDE that describes the aggregated traffic flow dynamics. Deriving the equilibrium often involves strong assumptions that may not hold in real-world traffic. For example, drivers are assumed to make decisions based on the position and speed of all other vehicles, whereas both human drivers and AVs rely only on neighboring traffic information due to the limited vision and wireless communication ranges, respectively (Li et al., 2025). Moreover, solving the coupled forward-backward PDEs can impose a high computational burden.

The second approach models mixed-autonomy traffic by adapting key parameters of existing traffic-flow models, such as the fundamental diagram, according to microscopic AV-controller design such as controller gains (Martínez and Jin, 2020) and AV penetration rate (Qin et al., 2021; Vander Laan and Schonfeld, 2020). The formulated model retains the structure of classical flow models, enabling the application of established analytical properties and numerical schemes. Related studies have adopted the first-order Lighthill-Whitham-Richards (LWR) model (Vander Laan and Schonfeld, 2020; Qin et al., 2021) and the second-order Aw-Rascle-Zhang model (Aw and Rascle, 2000; Zhang, 2002; Imran et al., 2024; Hui and Zhang, 2024) to analyze mixed traffic. Related results have derived how the microscopic control design affect macroscopic model parameters under ideal cases with known vehicle dynamics and spatial distributions of vehicle positions along the road. However, these models treat all vehicles as a homogeneous group and provide limited insight, and sometimes are inconsistent with, how AVs interact with surrounding traffic on microscopic levels.

To explicitly model the behavioral differences and interactions between AVs and HVs, two-class models have been proposed (Logghe and Immers, 2008; Zhang et al., 2024). Each class's density follows its own continuity equation, while its desired speed depends on the total density. In two-class models, all HVs are categorized to one class and all AVs to the other. As an extension to incorporate heterogeneity within AVs or HVs, multi-class models have also been proposed (Wong and Wong, 2002; Ngoduy and Liu, 2007; Levin and Boyles, 2016; Qian et al., 2017). Multi-class models characterize AVs and HVs using class-averaged attributes, assuming homogeneous behavior within each class. However, by analyzing real-world trajectory data, we show that within-class heterogeneity can exceed the differences between AVs and HVs. Therefore, a binary categorization of vehicles as AVs or HVs is inadequate to characterize traffic heterogeneity at the macroscopic level.

To address the limitations of discrete classification in capturing within-class heterogeneity, we represent driver characteristics using continuous-valued attributes. We first quantify microscopic driving heterogeneity through car-following model parameters and behavioral stochasticity. We then introduce a flow attribute variable that serves as a bridge between microscopic and macroscopic representations of traffic heterogeneity. Governed by a conservation law, the flow attribute remain invariant along vehicle trajectories. In Lagrangian coordinates, it reflects the driver's intrinsic behavioral characteristics, whereas in Eulerian coordinates, it represents the average driver attributes at a given spatiotemporal location. In previous studies, the model has been known as the Generic Second-Order Model (GSOM) (Lebacque et al., 2007). Several physical interpretations have also been proposed for the traffic flow attribute variable, such as the desired gap (Zhang et al., 2009) or the free-flow speed (Fan et al., 2014; Mo et al., 2024). However, existing reconstruction methods still operate at the macroscopic level and require complete spatiotemporal data, leading to high computational costs and limited feasibility for real-time applications. Moreover, under a macroscopic framework, it remains unclear how microscopic vehicle motions affect macroscopic flow attributes. In this paper, we propose reconstruction methods to obtain the flow attribute variable from vehicle trajectory data with a low computational cost and high interpretability.

1.2. Data collection and utilization in mixed-autonomy traffic

Traffic data are essential for reconstructing and calibrating traffic-flow models. Early-stage data collection methods, such as those used in the PeMS dataset (Choe et al., 2002), rely on road-based radars or loop detectors to measure vehicle flow and occupancy at fixed locations. Despite their ease of implementation, the data provided by these methods lacks detailed information on vehicle motion within a road segment and is thus insufficient for studying mixed autonomy traffic. With advancements in visual sensing techniques, traffic data across an entire road segment over a time period has been collected using surveillance cameras (e.g., the NGSIM FHWA, 2007 and I24 Motion Gloudemans et al., 2023 datasets) or aerial videos from helicopters (e.g., the HighD dataset Gloudemans et al., 2023). These sensors are fixed and provide video images in Eulerian coordinates, from which detailed vehicle trajectories can be extracted. However, trajectory extraction from video images is computationally intensive. Occlusions caused by infrastructure or adverse weather may further degrade data quality or result in (Gloudemans et al., 2023). Finally, these data do not reliably distinguish AVs from HVs.

Lagrangian data directly provides high-accuracy vehicle motion information, thereby significantly facilitating the analysis of microscopic traffic dynamics. The growing deployment of AVs is expected to provide abundant traffic data in Lagrangian coordinates. AVs are typically equipped with various onboard sensing devices, such as radar and LiDAR sensors, cameras, GPS, and Inertial Measurement Units (IMUs), which provide accurate real-time measurements of position, speed, acceleration of the ego vehicle and also surrounding vehicles (Liu et al., 2024; Masello et al., 2022). Several research groups and companies have released trajectory datasets collected by AVs in real-world traffic environments (Sun et al., 2020b; Zhou et al., 2024; Ammourah et al., 2025; Makridis et al., 2021).

Meanwhile, several studies have deployed designed controllers on experimental vehicles and tested their performance in terms of stability (Jin et al., 2018; Zhou et al., 2022; Hayat et al., 2025; Wang et al., 2023) and safety (Alan et al., 2024; Batkovic et al., 2023). In addition, some studies utilize commercial autonomous vehicles to collect traffic data or directly analyze open datasets to investigate the impact of AVs on traffic systems. Research has analyzed the effects of AVs from various aspects, such as string stability (Gunter et al., 2019, 2020; Yu and Yeo, 2025), safety (Zhang et al., 2025), mobility (Zhou et al., 2024; Beigi et al., 2025), fuel consumption (Mao et al., 2024), human's reaction to autonomous driving (Wen et al., 2022), calibration of AV dynamics (Hu et al., 2022; Li et al., 2021), and comparison between driving behaviors of AVs and HVs (Hu et al., 2023; Li et al., 2024). However, since the detection range of onboard sensors is typically restricted to a few nearby vehicles, the collected data fail to cover a complete spatiotemporal domain, which is essential for studying macroscopic mixed-autonomy traffic flow dynamics, i.e., the aggregated impact of AVs on traffic.

For mixed-autonomy traffic modeling, large-scale Eulerian datasets with reliable vehicle automation labels remain scarce. Recent efforts, including the TGSIM dataset (Ammourah et al., 2025) and the 100-CAV experiment (Lee et al., 2025; Ameli et al., 2025), have begun to provide empirical observations of AV operations in real traffic. However, the aggregate effects of AVs remain difficult to assess because current deployments involve limited penetration rates, spatial coverage, and observation periods. Even as AV deployment increases, constructing labeled Eulerian datasets will remain challenging, since external observations generally cannot determine whether a vehicle is automation-capable or whether its automated-driving functions are active. Given these challenges, existing validation methods relying on Eulerian data may not be feasible for mixed-autonomy flow model research.

1.3. Contribution

In conclusion, the main challenges in mixed-autonomy flow modeling lie in: 1) how to quantify heterogeneity at both the microscopic (driver behavioral) level and the macroscopic (aggregated flow) level; and 2) the mismatch between the availability of Lagrangian data and the need to validate Eulerian macroscopic flow models.

The main contributions of this work are twofold in bridging the gap: 1) we characterize heterogeneity in mixed traffic at the microscopic level through driver attributes and at the macroscopic level through a flow attribute; 2) we propose two reconstruction methods to infer the macroscopic traffic-heterogeneity attribute from Lagrangian vehicle trajectories, including a physics-based formulation for data-rich settings with historical trajectories and a neural-network approximation for data-scarce settings where only local spatiotemporal trajectories are available, as shown in Fig. 1. Our detailed findings are summarized as follows:

- Section 2: Analyzing heterogeneous attributes of AVs and HVs at the microscopic level. We analyze real AV and HV trajectories and identify two types of driver attributes that remain approximately constant during the driving process: the driver's microscopic motion dynamics model parameters and local behavioral uncertainty. We demonstrate that heterogeneity exists not only between AVs and HVs, but also within each of these classes. Moreover, the heterogeneity of two individual vehicles may exceed the difference between the AV-class average and HV-class average.
- Section 3: Modeling mixed autonomy traffic via a continuous-valued flow attribute variable. The heterogeneity within AV and HV classes implies that a discrete classification between them is improper, which motivates us to use a continuous-valued flow heterogeneity attribute variable to model mixed autonomy dynamics. We describe dynamics of the flow attribute variable via a conservation law of density weighted attribute. Therefore, the mixed-autonomy flow model is formulated by two conservation laws: one for vehicle number and the other one for flow attribute. This formulation provides a physically interpretable link between individual driving behaviors and macroscopic traffic flow.
- Section 4: Reconstruction of traffic flow attributes from vehicle trajectories when historical data is available. We propose an interpretable reconstruction method that aggregates driver attributes extracted from the trajectory data into flow attributes. The proposed formulation enables analysis of how microscopic vehicle behaviors influence the fundamental diagram of macroscopic traffic. Using real traffic datasets, we demonstrate that the proposed method yields lower modeling error in traffic flow prediction.
- Section 5: Reconstruction of traffic flow attributes with scarce data. We develop a data-driven framework that reconstructs macroscopic traffic flow heterogeneity attribute directly from locally available trajectories, without requiring historical data, vehicle-type labels, or AV penetration information. This allows macroscopic analysis of mixed-autonomy traffic using currently available datasets, where experimental AVs sparsely travel with HVs. The proposed framework thus provides a practical tool for traffic

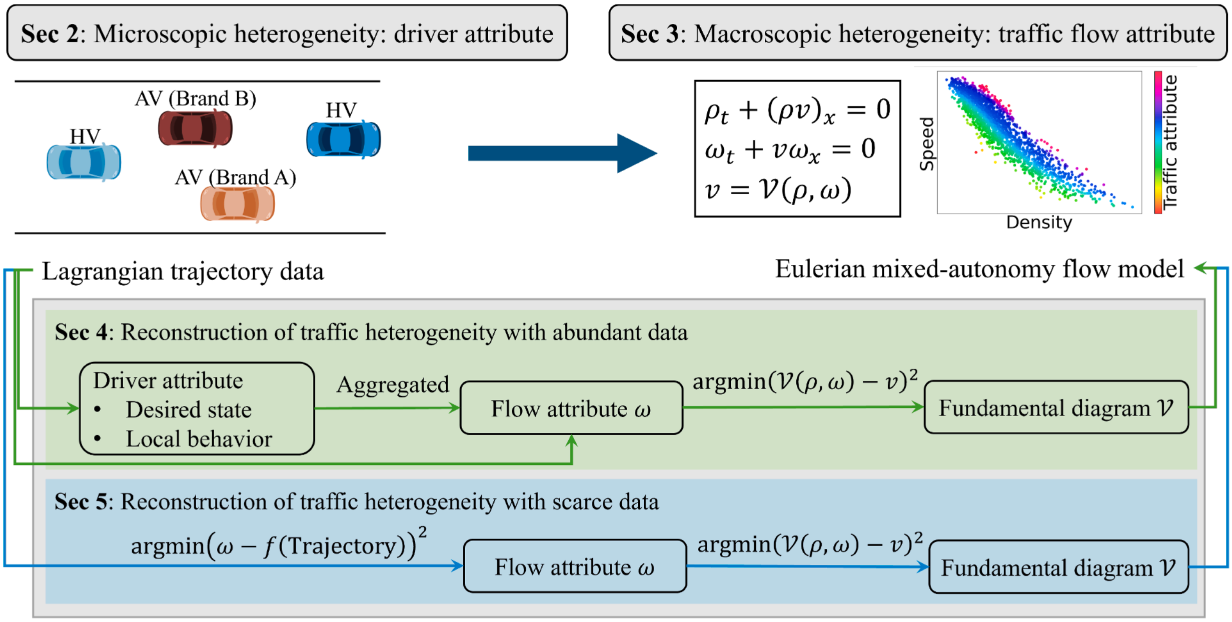

Fig. 1. We analyze heterogeneous driving behaviors at microscopic-level in Section 2 and introduce a traffic-heterogeneity attribute variable to explain how microscopic vehicle behaviors affect macroscopic flow dynamics in Section 3. We propose two reconstruction methods to obtain the flow attribute from vehicle trajectories: data-rich scenario with historical trajectory in Section 4 and data-scarce scenario only with trajectories in the current spatial-temporal cell in Section 5.

analysis and modeling in real-world mixed-autonomy traffic. Through experiments on multiple open-source traffic datasets, we show that the proposed method reduces calibration error from 20 % to 2 % and significantly closes the micro-macro gap. Further analysis validates that the proposed framework has a strong generalization ability and accurately captures flow attributes under previously unseen traffic conditions.

2. Microscopic heterogeneity as driver attribute

In this section, we extract microscopic-level vehicle motion attributes from real AV and HV trajectory data. We focus on longitudinal car-following motions in this paper. The research for lateral motion dynamics is one future work. We identify two driver-related attributes: a driver's driving dynamics model parameters, which reflects their preferred traffic state, and the variance in driving behavior, which captures their stochasticity. We show that there exists heterogeneity in the driving behaviors of the AV-class and HV-class. Besides, individual AVs and HVs also exhibit heterogeneous driving behaviors.

2.1. Driver attribute: car-following model parameters

The longitudinal driving decisions of human drivers are usually described by car-following models, which express the acceleration $\dot{v}$ as a function of speed v, gap s, and leading vehicle speed v_{leader}. Related studies have adopted several representative models such as optimal velocity model (OVM) and intelligent driver model (IDM) to analyze human driver behaviors. In this Section, we adopt the simple yet widely used OVM to characterize the microscopic heterogeneity of human drivers from real-world trajectories. We also show in Appendix B that with other choices of car-following models, the human drivers also present heterogeneous driving behaviors. The OVM model describes the vehicle motion as:

$$\dot{v} = \frac{V_{\text{opt}}(s) - v}{\tau} + \beta(v_{\text{leader}} - v), \tag{1}$$

where V_{opt} is the driver's desired speed dependent on its gap with the leader vehicle, τ is the adaption time to the desired speed, and β is the sensitivity parameter to the speed difference. We take the desired speed as:

$$V_{\text{opt}}(s) = \max\left\{0, \min\left\{V^{\text{f}}, \frac{s - s^0}{T}\right\}\right\}, \tag{2}$$

with V^{f} being the free-flow speed, T being the time gap, and s^0 being the minimum gap. The OVM clearly describes how a driver reacts to the three traffic states: its own speed v, the leader speed v_{leader}, and the gap s. The first term reflects how the driver adapts its acceleration based on gap, and the second term reflects how the driver adapts its acceleration based on the speed difference. Unlike human drivers, whose driving decisions are hard to be accurately captured, the motion of autonomous vehicles is governed by

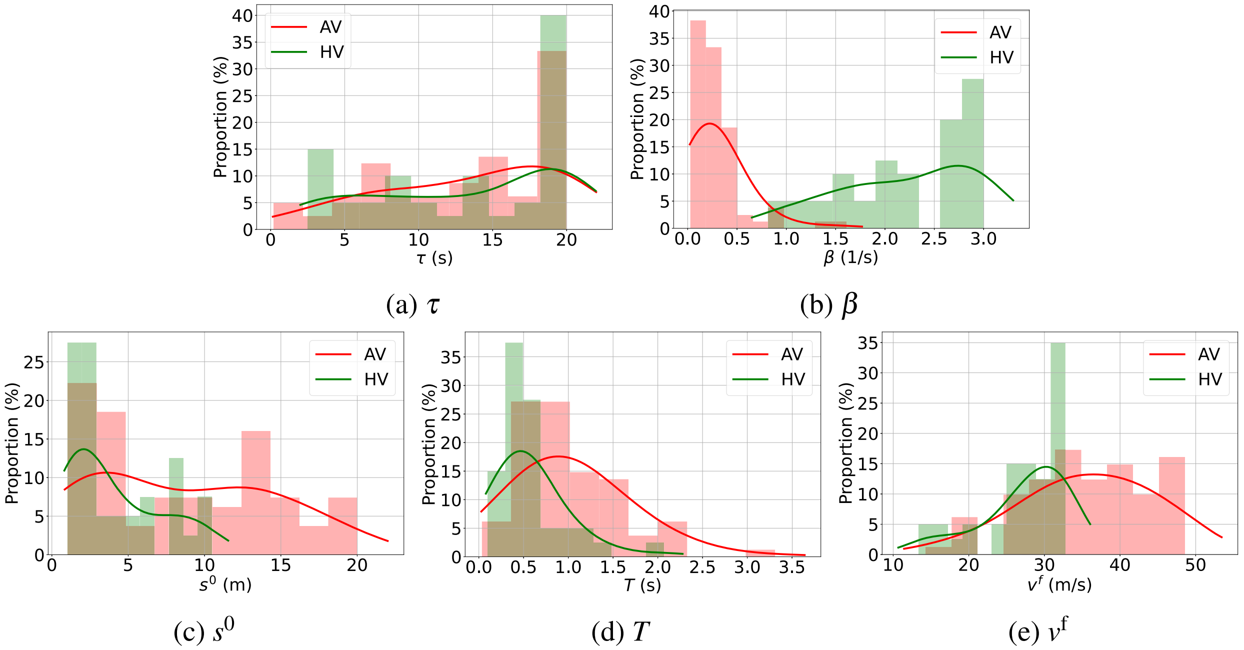

Fig. 2. Distribution of calibrated car-following model parameters for HV and AV. There exists heterogeneity not only in the AV-class and HV-class, but also within both classes.

well-designed controllers. However, the detailed controller algorithms in commercial AVs are often highly confidential. Therefore, we also calibrate an OVM car-following model as in Eq. (1) for autonomous vehicles.

Since we focus on the longitudinal dynamics in this section, we select the following datasets collected in varied car-following scenarios: Ring by Zheng et al. (2021), CATS collected by Shi and Li (2021), OpenACC from Makridis et al. (2021), and CentralOhio in Xia et al. (2023). The first dataset is collected from an experiment involving 40 human drivers on an 800-meter ring road. There is only one lane on the road, which eliminates the influence of lane-changing. The other three datasets are collected from AVs equipped with adaptive cruise control (ACC) operating in real traffic scenarios. We use the processed data provided in Zhou et al. (2024), which have extracted the trajectories of cruising behaviors. In Appendix A, we give the detailed introduction of these datasets and also the distribution of collected speed and gap information from the datasets. These datasets cover a wide range of traffic scenarios from free to congested, with the speed ranging from 0 m/s(fully stop) to 50 m/s (free flow) , and the gap ranging from to 5 m to 100 m. The calibrated free-flow speed V_f may exceed the observed speed range because it represents the desired speed under unconstrained free-flow conditions, whereas most calibration trajectories are collected under constrained car-following conditions.

We calibrate five parameters: τ, β, V^{f}, T, and s^0, from collected AV and HV trajectories. The detailed calibration algorithms are given in Appendix B. We give the distribution of calibrated parameters in Fig. 2. For AVs, we give the distribution of calibrated parameters for all AVs in the three AV datasets. From the parameter distribution, we conclude the following two findings:

- When HVs and AVs are considered as two distinct classes, significant differences can be observed between them across all five parameters. This observation is consistent with prior findings on the heterogeneity between AVs and HVs (Zhou et al., 2024). For example, in the distribution of the speed sensitivity parameter β shown in Fig. 2(b), the majority of AVs have $\beta < 1$, whereas most human drivers have $\beta > 1$. The smaller calibrated β values for AVs suggest that, within the OVM approximation, AV acceleration responses are less dominated by the instantaneous relative-speed term. This may reflect the effects of spacing/time-headway regulation, response smoothing, and safety constraints in commercial AV longitudinal control (Makridis et al., 2020; Yu and Yeo, 2025; Wang et al., 2025). Similarly, for the stopping distance s^0 in Fig. 2(c), some AVs adopt a conservative driving policy with s^0 values around 15-20 m, while most human drivers have s^0 values below 5 m.
- In addition to the heterogeneity between the HV class and the AV class, we also observe heterogeneity within each class. It is well understood that human drivers exhibit considerable variation in model parameters. Take the same example in Fig. 2(b), human drivers have speed sensitivity parameters β ranging from 1.0 to 3.0. Similarly, commercial AVs also exhibit noticeable variation in microscopic parameters. For example, the distribution of the gap-sensitivity parameter τ in Fig. 2(a) shows that both AVs and HVs have values ranging from 5 to 20.

The heterogeneity of each AV and each HV implies that it is improper to describe mixed-autonomy traffic via multi-class models that takes AV as a class and HV as another class, and motivates us to propose continuous-valued flow attribute variable in this paper.

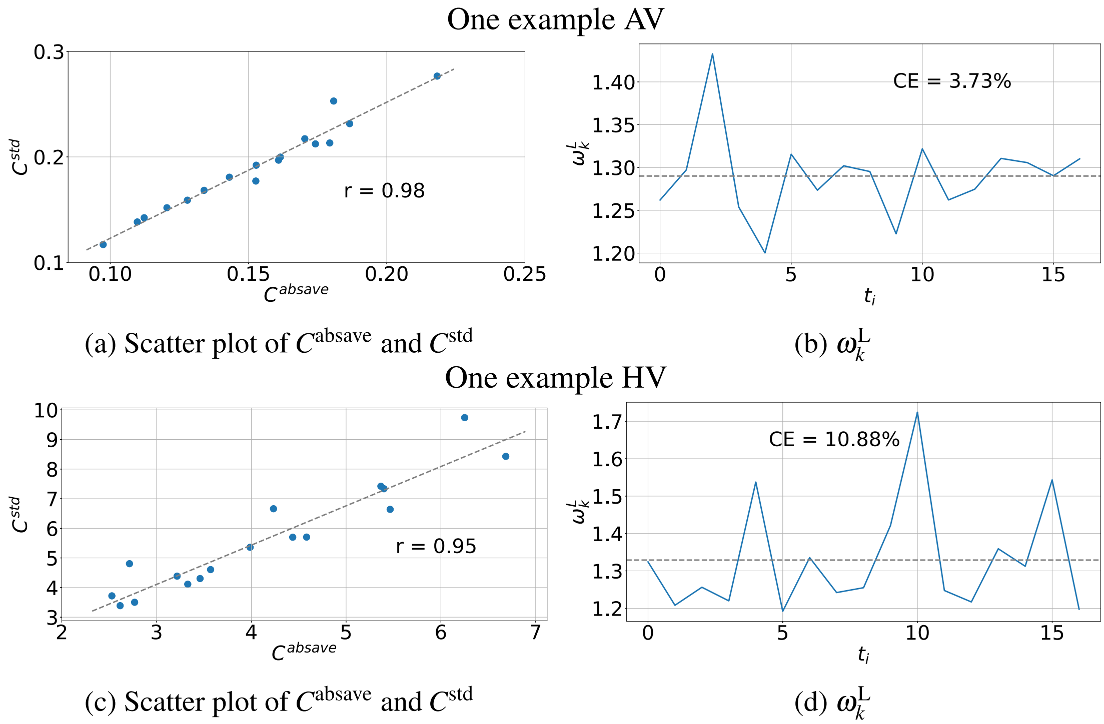

(a) Scatter plot of C^{absave} and C^{std} (b) ω_k^{L}

(c) Scatter plot of C^{absave} and C^{std} (d) ω_k^{L}

Fig. 3. The stochasticity-related driver attribute constructed from jerk profiles. There exists a linear relationship between the C^{absave} and C^{std} as shown in (a)(c). We calculate a vehicle-attribute value ω^{L} and plot the ω^{L} values during each trajectory segment period t_i as in (b)(d). The driver attribute also has a low constancy error(CE) and remains almost constant during the driving process. We give the result for one example AV and example HV of the CentralOhio dataset here. We further show in Fig. 4 that the proposed ω^{L} also remains a low CE for all vehicles over other datasets.

2.2. Driver attribute: stochasticity

While drivers have a desired speed, they also exhibit uncertainty in practice. We propose a jerk-based metric to represent the stochastic characteristics of drivers and demonstrate that it remains approximately constant during the driving process.

For a vehicle k, we divide it trajectory into n segments $\mathcal{T}_1, \mathcal{T}_2, \ldots, \mathcal{T}_n$. We consider the trajectory during the time segment i, and calculate the average absolute jerk:

$$C_k^{\text{absave}}(i) = \frac{1}{T_i} \sum_{t \in \mathcal{T}_i} |j_k(t)|, \tag{3}$$

and the standard deviation of its jerk:

$$C_k^{\text{std}}(i) = \sqrt{\frac{1}{T_i} \sum_{t \in \mathcal{T}_i} (j_k(t) - C_k^a(i))^2}, \tag{4}$$

where T_i is the number of sample data in the time segment, $j_k(t)$ is vehicle k's jerk at time t, and $C_k^a(i) = \frac{1}{T_i} \sum_{t \in \mathcal{T}_i} j_k(t)$. We find that for both AVs and HVs, there is a linear relationship between C_k^{absave} and C_k^{std}, as shown in Fig. 3(a) and in Fig. 3(c) respectively.

We solve a linear regression equation by the least-squares method as:

$$C_k^{\text{std}}(i) = a_k + C_k^{\text{absave}}(i) b_k. \tag{5}$$

For the example AV and HV given in Fig. 3, the correlation coefficients are 0.98 and 0.95 respectively, which indicates a strong linear correlation between the two jerk-related values. Based on the solved regression coefficient a_k, we further define vehicle-k's attribute at each time segment i as:

$$\omega_k^{\text{L}}(i) = \frac{C_k^{\text{std}}(i) - a_k}{C_i^{\text{absave}}(i)}. \tag{6}$$

We find that the value of ω_k^{L} remains approximately constant during driving, as shown in Fig. 3(b) and (d). To quantitatively evaluate how much the ω_k^{L} varies during the driving process, we define a *constancy error* as:

$$CE_k = \frac{1}{n} \sum_i \left(\frac{\omega_k^{\text{L}}(i) - \omega_k^{\text{L}}}{\omega_k^{\text{L}}} \right)^2 \times 100\,\%, \tag{7}$$

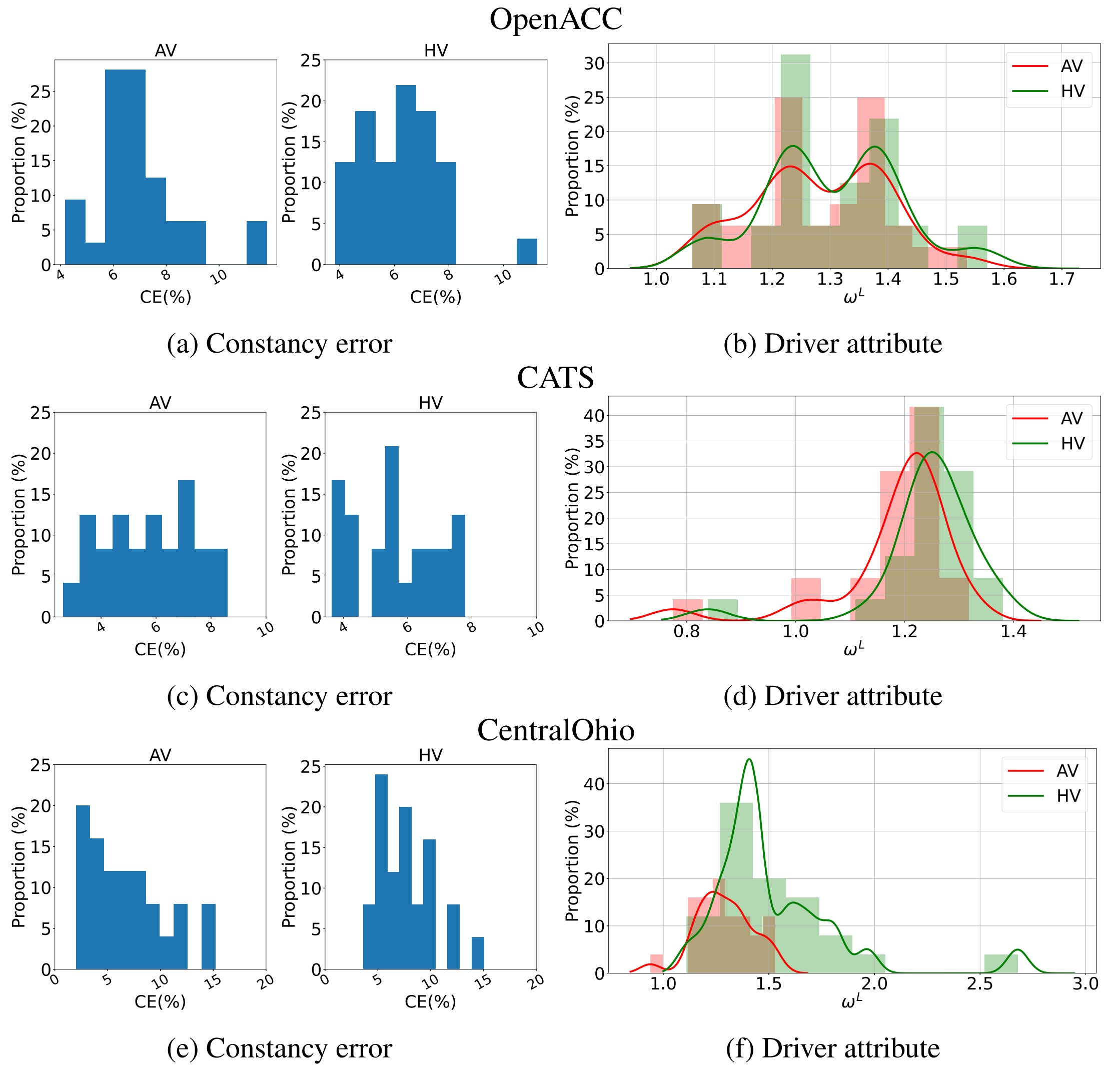

Fig. 4. We extract the driving stochasticity-related attribute from the jerk profile for the three datasets. The first column gives the distribution of constancy error (CE) of the proposed vehicle-attribute ω^{L}. Most vehicles have CE less than 10 %, which indicates that the ω^{L} remains almost constant and is a metric of driver attributes. The right column compares the distribution of ω^{L} for HVs and HVs. As the figures show, there is both inter-class heterogeneity (when we treat AVs as a class and HVs as another class) and intra-class heterogeneity (when we analyze AVs or HVs individually).

with $\omega_k^{\mathrm{L}} = \frac{1}{n}\sum_i \omega_k^{\mathrm{L}}(i)$ being vehicle-k's attribute value averaged over the whole driving process. The CE for the example AV and HV are 3.73 % and 10.88 % respectively. To demonstrate that the proposed jerk-based value ω^{L} is a driver attribute for all vehicles, we give in Fig. 4(a)(c)(e) the constancy error CE_k for all AVs and HVs in the three AV datasets. We see that the constancy error is distributed between 2 % and 20 %, which indicates that for both AVs and HVs, the extracted ω_k^{L} by Eq. (6) has only a small variation during driving, and thus can be regarded as a driver attribute.

We now analyze the differences in driving behavior between AVs and HVs. Fig. 4(b)(d)(e) present the distribution of ω_k^{L} for all AVs and HVs. The results reveal both inter-class heterogeneity (between AVs and HVs) and intra-class heterogeneity (among AVs or HVs individually).

- When treating AVs and HVs as two distinct groups, they exhibit different distribution patterns. For example, in the CentralOhio dataset shown in Fig. 4(f), most human drivers have $\omega_k^{\mathrm{L}} \geq 1.3$, whereas a majority of AVs have $\omega_k^{\mathrm{L}} \leq 1.2$. Similarly, in the CATS dataset Fig. 4(d), HVs exhibit values around 1.3, while the AV group centers from 1.1 to 1.2.
- At the individual level, the behavioral differences between two AVs or two HVs may be even larger the average difference between the two classes. For instance, in the OpenACC dataset shown in Fig. 4(b), the class averages for AVs and HVs are both around 1.2. However, given the full distribution range from 1.0 to 1.6, the difference between two individual vehicles can be greater than the class-level average difference. These findings suggest that it is inappropriate to simply classify AVs and HVs into discrete groups. Consequently, traditional multi-class traffic flow models are insufficient for capturing such within-class heterogeneity.

In conclusion, the analysis on the microscopic level highlights that the heterogeneity between individual vehicles within the class, regardless of AVs or HVs, can exceed the average inter-class heterogeneity, which motivates the use of a continuous-valued flow attribute over discrete multi-class models.

3. Macroscopic heterogeneity as traffic flow attribute

Motivated by the observation that heterogeneous microscopic behaviors arise not only between AVs and HVs but also within each class, we introduce a continuous-valued flow attribute to model mixed-autonomy traffic and, more importantly, propose reconstruct methods to obtain this attribute from data.

In macroscopic traffic flow modeling, the three basic variables are density ρ, flow q, and traffic speed $v = q/\rho$. The density and flow are defined as the number of vehicles per unit length and per unit time respectively. By the definition, these variables provide information on 'how many' vehicles, but not 'what type' of vehicles. To reflect the vehicle behaviors at a macroscopic level, we introduce a traffic flow attribute variable ω, and formulate the traffic flow dynamics as:

$$\partial_t \rho + \partial_x(\rho v) = 0, \tag{8}$$

$$\partial_t \omega + v\partial_x \omega = 0, \tag{9}$$

$$v = \mathcal{V}(\rho, \omega), \tag{10}$$

where traffic speed $v(t,x)$ is determined by the density $\rho(t,x)$ and traffic flow attribute $\omega(t,x)$ through the two-variable fundamental diagram $\mathcal{V}(\rho,\omega)$. This model is refereed to as the generic second-order model (GSOM) in related work (Lebacque et al., 2007). If we set $\mathcal{V}(\rho,\omega) = \omega - p(\rho)$ by a suitable pressure function $p(\rho)$, the GSOM becomes the ARZ model. If we assume that $\omega(t,x)$ remains a constant value in the whole spatial-temporal domain, then the GSOM becomes the LWR model. In related research, several interpretations and corresponding reconstruction methods for the ω value has been proposed (Zhang et al., 2009; Fan et al., 2014; Mo et al., 2024), but they have a high computation cost that cannot be applied to real-time traffic application.

Remark 1 (Physical interpretation of GSOM as conservation laws)**.** The Eq. (8) is a conservation law of vehicle mass. For a road segment of length L without any ramps, the number of vehicles on the road is $N = \int_0^L \rho(t,x)\mathrm{d}x$, and the first PDE in Eq. (8) is equivalent as $\dot{N}(t) = Q_{\mathrm{in}}(t) - Q_{\mathrm{out}}(t)$, with $Q_{\mathrm{in}}(t)$ and $Q_{\mathrm{out}}(t)$ being the entering and exiting flux. The second PDE Eq. (9) in the GSOM can also be written as a conservation law. Combining Eqs. (8) and (9) yields:

$$\partial_t(\rho\omega) + \partial_x(\rho\omega v) = 0. \tag{11}$$

The equation shows that the density-weighted traffic flow attribute also satisfies the conservation law. We further define $I(t) = \int_0^L \rho(t,x)\omega(t,x)\mathrm{d}x$, and we have $\dot{I}(t) = A_{\mathrm{in}}(t) - A_{\mathrm{out}}(t)$, with $A_{\mathrm{in}}(t) = v(t,0)\rho(t,0)\omega(t,0)$ and $A_{\mathrm{out}}(t) = v(t,L)\rho(t,L)\omega(t,L)$ being the weighted attributes entering and exiting the road segment. The first conservation law describes that the vehicle number is decided by "how many" vehicles enter and exit the road, and the second conservation law shows that the dynamics of the traffic flow attribute are determined by the entering and exiting attributes, i.e., the drivers "who" enter and exit the road.

To make the GSOM model applicable in practice, it is essential to solve the following two problems. First, how to design a reconstruction method to get the traffic flow attribute from vehicle trajectories. Given a road, we divide the spatial-temporal range to several cells i. We denote $\mathcal{N}_i$ as the set of vehicles in the cell i. For each cell i, analogous to Edie's formulation of traffic density $\rho_i = \frac{1}{\text{Cell area}} \sum_k \text{Travel time of vehicle } k \text{ in the cell}$, flow $q_i = \frac{1}{\text{Cell area}} \sum_k \text{Travel length of vehicle } k \text{ in the cell}$, and the spatial-temporal average speed $v_i = q_i/\rho_i$, we find a reconstruction mapping f from the vehicle trajectory to the flow attribute in a generic formulation as:

$$\omega_i = \sum_{k \in \mathcal{N}_i} f(\text{Vehicle } k \text{ motion information, such as speed, gap, acceleration}). \tag{12}$$

Second, how to calibrate the fundamental diagram $\mathcal{V}(\rho,\omega)$ from data. Assume that there are collected trajectories from a series of spatial-temporal cells i as in Fig. 5 and corresponding reconstructed flow density ρ_i, speed v_i, and flow attribute ω_i, we aim to calibrate the fundamental diagram via solving the constrained optimization problem:

$$\arg\min_{\theta} \sum_i \left(\hat{\mathcal{V}}(\rho_i, \omega_i; \theta) - v_i\right)^2 \tag{13}$$

$$\text{s.t.} \quad \hat{\mathcal{V}}(\rho,\omega;\theta) \geq 0, \tag{14}$$

$$2\partial_\rho \hat{\mathcal{V}}(\rho,\omega;\theta) + \rho\partial_{\rho\rho}\hat{\mathcal{V}}(\rho,\omega;\theta) \leq 0, \tag{15}$$

with θ being parameters in the fundamental diagram. The objective function Eq. (13) is to minimize the calibration error. The two constraints are imposed to ensure well-posedness of the GSOM model. The constraint (14) requires that the traffic speed is non-negative, and the constraint (15) requires that the flow $Q = \rho\mathcal{V}(\rho,\omega)$ is concave.

Sections 4 and 5 formulate the trajectory-flow mapping and fundamental diagram calibration under data-rich and data-scarce scenarios respectively. In the data-rich scenario, we assume that there are enough historical trajectory for all vehicles to calibrate their driver attributes, as in Fig. 5(a). And we propose a reconstruction formulation to get the flow attribute from the driver attribute and current trajectories. While in the data-scarce scenario as in Fig. 5(b), only trajectory in the studied spatial-temporal cell is available, and we aim to find a mapping from current trajectory to the flow attribute.

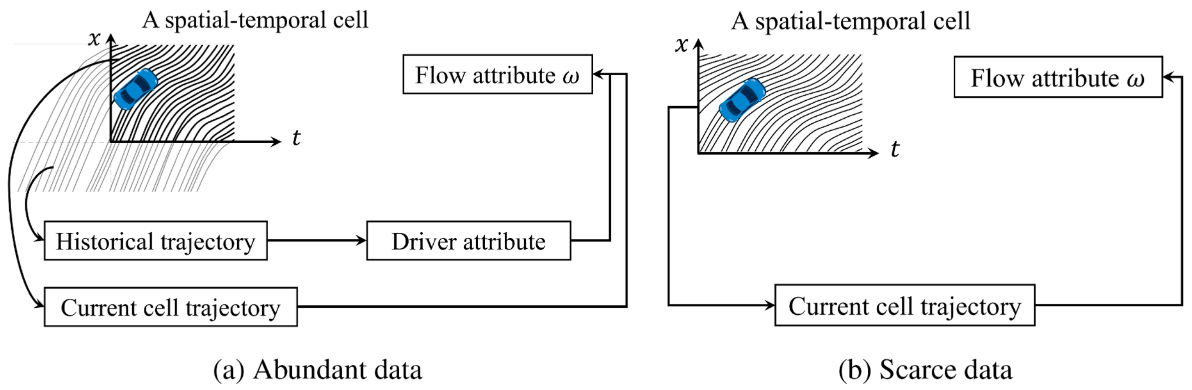

Fig. 5. We reconstruct flow attributes with abundant data and scarce data. In the abundant data scenario, there are enough historical trajectories for all vehicles to calibrate the driver attributes, which are used to reconstruct the flow attribute. In the more challenging scarce data scenario, we only have trajectories within the current spatial-temporal cell.

4. Reconstruction of traffic heterogeneity with abundant data

In this section, we focus on scenarios with abundant traffic data and propose a formulation to get the traffic flow attribute from vehicle trajectories. Due to the lack of real large-scale mixed-autonomy data, we validate the proposed flow model and reconstruction method on real heterogeneous HV data from the experiment on a single-lane in Zheng et al. (2021). As analyzed in Section 2, the heterogeneity within HVs may be even larger than that between HVs and AVs. So the validation still provides insights for future research if large-scale mixed-traffic data becomes available.

4.1. Reconstruction of traffic heterogeneity from driver heterogeneity

In this section, we aim to find a mapping from trajectories to flow attributes with explicitly interpretable formulation. We focus on single-lane traffic where drivers only have car-following dynamics. Corresponding to the general formation of micro-macro reconstruction in Eq. (12), we propose a specific formulation to calculate the flow attribute ω_i for a spatial-temporal cell i as:

$$\omega_i = \underbrace{\frac{1}{N_i}\sum_{k\in\mathcal{N}_i} V_k^{\mathrm{f}}/V}_{\text{Driver attribute}} + \underbrace{\frac{1}{\sum_{k\in\mathcal{N}_i} e^{-\omega_k^{\mathrm{L}}}}\sum_{k\in\mathcal{N}_i} e^{-\omega_k^{\mathrm{L}}}\left(V_{i,k} - V_{i,k}^{\mathrm{desired}}\right)/V}_{\text{Driver's local behavior with interactions in traffic}}, \tag{16}$$

where $V_{i,k} = X_{i,k}/T_{i,k}$ is vehicle k's local spatial-temporal average speed in the cell i with $X_{i,k}$ and $T_{i,k}$ being the distance and time vehicle-k travels in the cell, V_k^{f} is vehicle k's free-flow speed, and $V_{i,k}^{\mathrm{desired}} = \max\left\{0, V_k^{\mathrm{opt}}\left(\frac{1}{\rho_i} - l_k\right)\right\}$ is vehicle k's gap-dependent desired speed given current traffic density ρ_i with l_k being its length. In the reconstruction formulation Eq. (16), corresponding to the general formulation Eq. (12), the $V_{i,k}$ is calculated from current trajectory, and ω_k^{L}, V_k^{f}, $V_{i,k}^{\mathrm{desired}}$ are driver attributes from historical trajectories as we have shown in Section 2. The $V > 0$ is a constant value representing the speed to render that the constructed ω is dimensionless and thus is consistent with Section 5. To explain the intuition and rationale behind the two terms in Eq. (16), we begin by analyzing collected traffic data.

We divide the 40 drivers into four groups: Group One (Drivers 1-10), Group Two (Drivers 11-20), Group Three (Drivers 21-30), and Group Four (Drivers 31-40). For Group One, we select cells containing all ten drivers and mark the corresponding density-speed scatter points in red in Fig. 6(a). For the other three groups, we follow the same procedure and mark their density-speed scatter points in Fig. 6(a). From Fig. 6(a), we have two key findings:

1. For Group One, its macroscopic average speed is higher than that of the other groups at the same density. Moreover, Group one maintains a higher speed at almost the entire range of densities.
2. For each Group, the speed also varies at the same density. Take Group One as an example, when the density is approximately 40 veh/km, the observed speed ranges from 45 km/h to 55 km/h.

The two terms in the reconstruction of ω in Eq. (16) are designed based on the above two findings. The first finding indicates that some vehicles consistently exhibit higher speed regardless of density, which motivates the first term in Eq. (16) to capture such density-independent speed trends. We calculate the average free-flow speed V_k^{f} for Group One to be 30 m/s; while for other groups, it is around 27 m/s. For the second term in Eq. (16), we note that $V_{i,k}$ is vehicle k's *actual* speed, while $V_{i,k}^{\mathrm{desired}}$ represents its *desired* speed at density ρ_i. The difference $\Delta V_{i,k} = V_{i,k} - V_{i,k}^{\mathrm{desired}}$ reflects the *aggressive speed* presented by driver k in current traffic conditions. With a larger $\Delta V_{i,k}$, driver k tends to drive faster, and thus the corresponding (ρ, v) point will move upward in the fundamental diagram. We also note that for vehicle k, a higher ω_k^{L} implies more uncertainty in its driving behavior. So even if a driver has a larger $\Delta V_{i,k}$, it may result from its more uncertain driving behavior, and thus it should contribute less to the cell value ω_i.

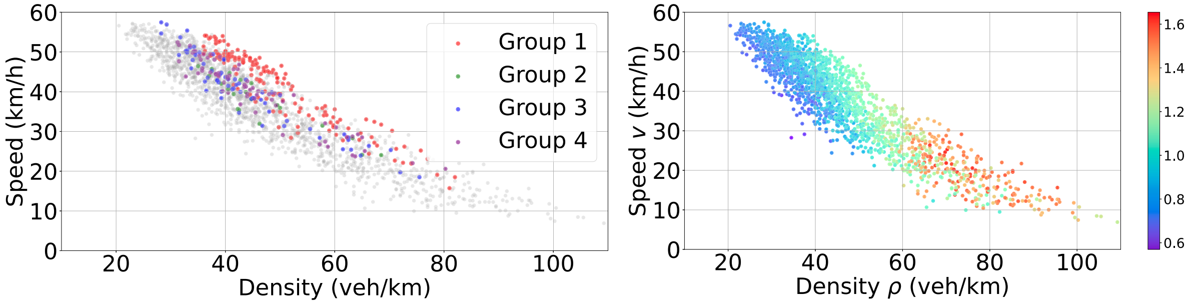

(a) The speed-density scatter points for four vehicle groups (b) The speed-density scatter points with continuous-valued flow attribute

Fig. 6. Subfig(a): The scatter speed-density points for four vehicle groups. The grey points are the speed-density $v-\rho$ points for the whole spatial-temporal domain. Since we select cells with all vehicles in the corresponding group, there are cells unlabeled. Subfig(b): The speed-density $v-\rho$ scatter plot with the continuous-valued flow attribute ω.

We give the speed-density ($v-\rho$) scatter plot in Fig. 6(b). For the same density ρ, the scattered speed is approximately separated by the reconstructed ω. The observed separation shows the potential to calibrate a fundamental diagram $\mathcal{V}(\rho,\omega)$ using ρ and ω as two independent variables, which will give present a lower calibration error than the traditional one-dimensional $V(\rho)$.

4.2. Calibration of two-variable fundamental diagram

In this subsection, we calibrate a two-variable fundamental diagram $\mathcal{V}(\rho,\omega)$ to capture the dependency of traffic speed on density ρ and flow attribute ω by solving the constrained optimization problem in Eq. (13). Traditional optimization-based fitting methods, such as polynomial regression or parametric curve fitting, require a pre-determined functional form. In our case, the fundamental diagram $\mathcal{V}(\rho,\omega)$ involves interactions between density ρ and heterogeneous driver attributes ω, which may not be easily captured by fixed-form models. In contrast, neural networks (NNs) offer greater flexibility since there is no assumptions on the functional form of the fundamental diagram. Therefore, we adopt a neural network to learn the mapping from (ρ,ω) to v, allowing for accurate calibration without relying on restrictive assumptions about the underlying functional structure. The effectiveness of NN-based calibration for single-variable fundamental diagram has been shown in our previous work (Zhao and Yu, 2024). In this paper, we further extend to calibrate the two-variable fundamental diagram $\mathcal{V}(\rho,\omega)$.

We convert the constrained optimization problem in Eq. (13) to an unconstrained problem using the penalty method and train the neural network by minimizing the loss function:

$$L(\theta)=L_d(\theta)+pL_p(\theta), \tag{17}$$

where the data loss L_d and the penalty loss L_p are calculated based on the objective function and constraints in Eq. (13), and $p>0$ is a penalty coefficient. To evaluate the calibration accuracy, we randomly select N_d points (ρ_i,ω_i,v_i) from all reconstructed (ρ,ω,v) in the whole spatial-temporal domain, and get the data loss L_d as the difference between the learned speed $\hat{\mathcal{V}}(\rho_i,\omega_i)$ and observed speed v_i:

$$L_d=\frac{1}{N_d}\sum_{i=1}^{N_d}(\hat{\mathcal{V}}(\rho_i,\omega_i;\theta)-v_i)^2. \tag{18}$$

To constrain the learned fundamental diagram, we randomly select N_p points of (ρ_j,ω_j) with $\rho_i\in[0,\rho_{\max}]$, $\omega_j\in[\omega_{\min},\omega_{\max}]$ and get the penalty loss as:

$$L_p=\frac{1}{N_p}\sum_{j=1}^{N_p}\left(\min\left\{0,\hat{\mathcal{V}}(\rho_j,\omega_j;\theta)\right\}\right)^2+\frac{1}{N_p}\sum_{j=1}^{N_p}\left(\max\left\{0,2\partial_\rho\hat{\mathcal{V}}(\rho_j,\omega_j;\theta)+\rho_j\partial_{\rho\rho}\hat{\mathcal{V}}(\rho_j,\omega_j;\theta)\right\}\right)^2. \tag{19}$$

The partial derivatives $\partial_\rho\mathcal{V}$ and $\partial_{\rho\rho}\mathcal{V}$ are calculated using the automatic differentiation provided by the TensorFlow. The first term in L_p constrains that the fundamental diagram always have non-negative speed as required in Eq. (14), and the second term is designed to ensure hyperbolicity of the traffic-flow dynamics by enforcing a concave fundamental diagram as required in Eq. (15). When evaluating the penalty loss, the choice of the points (ρ_j,ω_j) is independent of the points (ρ_i,ω_i) that are used to evaluate the data loss L_d.

We set the NN as a fully connected feedforward neural network with 3 hidden layers and 50 neurons in each hidden layer. The input dimension of the NN is two, one for density and one for flow attribute. The output of the NN is traffic speed. We run 50,000 epochs of the ADAM optimizer to train the NN. To evaluate the data loss, we randomly select 60 % points from all reconstructed (ρ,v,ω) data. To evaluate the penalty loss, we select 200 (ρ,ω) points uniformly distributed within the range $[0,\rho_{\max}]\times[\omega_{\min},\omega_{\max}]$. We set the penalty coefficient p as 1,000. We have found that the result is less sensitive to the choice of p, and a larger p such as

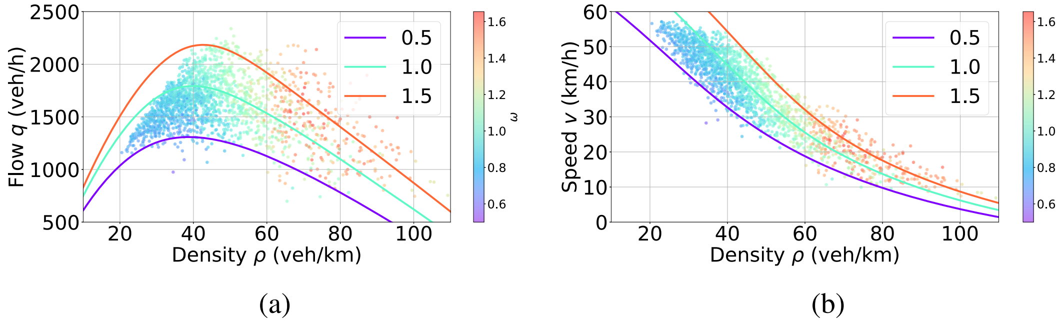

Fig. 7. The calibrated fundamental diagram.

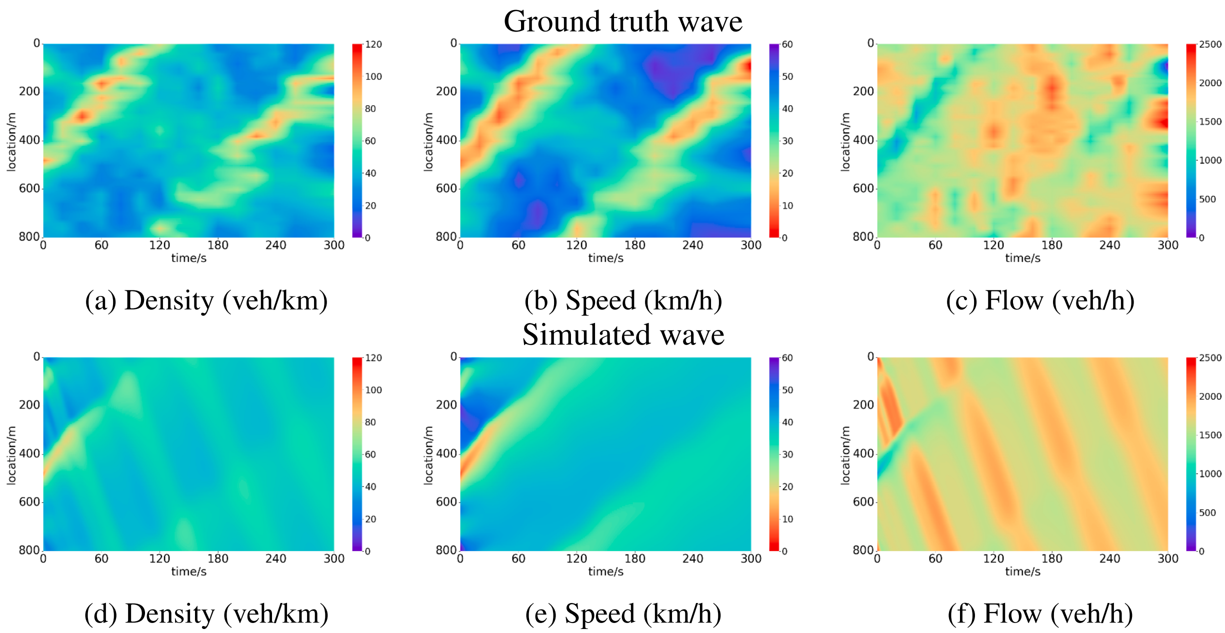

Fig. 8. The ground-truth traffic wave and simulated trajectories via the GSOM model.

Table 1
The simulation error for the wave propagation using the ARZ and GSOM model.

	Density	Speed	Flow
ARZ	30.86 %	30.18 %	15.06 %
GSOM	25.77 %	24.36 %	14.09 %
Accuracy improvement	17.49 %	19.28 %	6.44 %

10,000 and 50,000 has only margin effect on the learned fundamental diagram. To ensure consistency and robustness across datasets, we apply min-max normalization to the input variables of ρ and ω. The normalization ensures stable neural network training and facilitates generalization to datasets with different resolutions and scales (Huang et al., 2023).

We divide the full spatial-temporal domain into $N_x \times N_t$ cells, and we evaluate the calibration error using the root-mean squared error (RMSE):

$$E_{FD} = \sqrt{\frac{1}{N_x N_t} \sum_i \left(\frac{\hat{\mathcal{V}}(\rho_i, \omega_i; \theta) - v_i}{v_i} \right)^2} \times 100\,\%. \tag{20}$$

We get the calibration error as $E_{FD} = 12.2\,\%$, which shows that the two-variable fundamental diagram provides an accurate calibration of traffic systems. We present the calibrated fundamental diagram in Fig. 7. We also numerically solve the GSOM Eqs. (8)-(9) with the learned fundamental diagram. We denote the simulated density, speed and flow as $\hat{\rho}$, $\hat{v}$, $\hat{q}$ respectively. We set the initial condition $\hat{\rho}(0,x)$ and $\hat{\omega}(0,x)$ the same as observed data $\rho(0,x)$ and $\omega(0,x)$. Since it is a ring road, we use periodic boundary conditions. We give in Fig. 8 the ground truth and simulated traffic states. We see that the GSOM model captures the wave propagation. We quantitatively measure the model error as

$$E_Y = \sqrt{\frac{1}{N_x N_t} \sum_{i,j} \left(\frac{\hat{Y}_i - Y_i}{Y_i} \right)^2} \times 100\,\%, \tag{21}$$

with $Y = \rho, v, q$. We also run numerical simulations for the ARZ model and compare the model error for ARZ and GSOM in Table 1. As the results show, by considering traffic heterogeneity, the GSOM model provides a more accurate estimation of all three macroscopic traffic values: density, speed and flow. For example, the speed simulation error using the GSOM is reduced up to 20 %.

5. Reconstruction of traffic heterogeneity with scarce data

In the previous analysis, we design a micro-to-macro framework that reconstructs the flow attribute from current trajectories and microscopic driver attributes that are calibrated from historical trajectories. The previous analysis relies on trajectory data collected in experimental settings, where sufficient data are available for detailed behavioral analysis as in Fig. 5(a). However, in real-world traffic, vehicle trajectories are often observed over only short time intervals, and there is little or even no historical data available to construct accurate microscopic behavioral attributes. In this section, we further extend the proposed micro-to-macro formulation to scarce data traffic scenarios where only current trajectories are available as in Fig. 5(b).

We use the NGSIM (FHWA, 2007) and TGSIM (Talebpour et al., 2024) datasets. These datasets are collected in real highway, and therefore, for newly arrived vehicles, there are no available historical trajectories to calibrate the microscopic attributes. The NGSIM dataset is collected on the eastbound I-80 freeway in Emeryville, California, using video recordings. The segment is approximately 500 m long and consists of six lanes. Vehicle trajectories are provided at a temporal resolution of 0.1 s. We use the three datasets collected duing three 15-min time periods: 04:00-04:15, 05:00-05:15, and 05:15-05:30, which cover various traffic conditions ranging from free flow to congested regimes. The TGSIM dataset offers mixed-traffic driving scenarios using high-resolution 8K aerial videography from helicopters. We use three datasets: I90-I94 Stationary, I90-I94 Movings, and I294 L1. The I90-I94 Stationary dataset collects trajectory via a hovering stationary helicopter. This dataset covers a 1.3 km segment. Two SAE Level 2 ADAS-equipped vehicles are set to drive through the segment. The I90-I94 Moving dataset covers a 4 km long segment. Three SAE Level 2 ADAS-equipped vehicles travel on the road (one at a time). Once a vehicle finishes the segment, the helicopter will return to the beginning of the segment to follow the next SAE Level 2 ADAS-equipped vehicle. The I-294 L1 dataset covers a 4.8 km section of the Illinois Tollway with four lanes in each direction. Three SAE Level 1 ADAS-equipped vehicles travel as a vehicle chain.

5.1. Reconstruction of traffic heterogeneity from trajectory

In the data-scarce scenario, since there is little or even no historical trajectory data to calibrate the microscopic driver attributes as we have done in Eq. (16), we aim to find a mapping from current trajectories in the studied spatial-temporal cell to corresponding flow attributes as in Fig. 5(b). In the following studies, we treat multi-lane road as one general lane, and the spatial-temporal cells include vehicle trajectories on all lanes.

We get the micro-macro mapping via the following two-steps. First, we get ω value from collected $\rho - v$ data. Second, we build and learn a neural network that maps vehicles' behavior to traffic flow attributes. In the training process, the method follows a macro-then-micro procedure, i.e., we first analyze macroscopic traffic and then learn how microscopic driving behavior maps to macroscopic traffic flow attributes. But after we have finished the training process, the neural network works in a micro-then-macro step, i.e., we collect vehicles' driving trajectory and then get a traffic flow attribute value via forward propagation of the trained neural network. The detailed procedures of the two steps are introduced as follows.

In the first step, we assume that the ω value implies the scaling factor for speed, i.e., there exists a one-dimensional $V(\rho)$ such that

$$\mathcal{V}(\rho, \omega) = \omega V(\rho). \tag{22}$$

We solve the Eq. (13) and get the one-dimensional fundamental diagram $V(\rho)$. From the calibrated fundamental diagram $V(\rho)$, for each spatial-temporal cell indexed by i, we get the traffic flow attribute value ω_i as:

$$\omega_i = v_i / V(\rho_i). \tag{23}$$

The ω value is used as the ground-truth value to train a neural network that maps from microscopic trajectories to macroscopic flow attribute values.

In the second step, we build a neural network with trainable parameter θ_ω. The NN takes trajectory-related values as input and outputs the reconstructed traffic flow attribute ω value. For each cell i, we denote $\mathcal{N}_i$ as the set of vehicles that travel within the cell. For each vehicle $k \in \mathcal{N}_i$, we extract a trajectory feature vector $f_{i,k}$ from the collected trajectory. For each vehicle, the NN outputs a value $\hat{\omega}(f_{i,k}; \theta_\omega)$ that reflects how these driver attributes affect the traffic flow dynamics. The overall flow attribute value in a cell i is the sum of attributes of all vehicles within the cell, i.e., the NN estimated traffic flow attribute is

$$\hat{\omega}_i(\theta_\omega) = \sum_{k \in \mathcal{N}_i} \hat{\omega}(f_{i,k}; \theta_\omega). \tag{24}$$

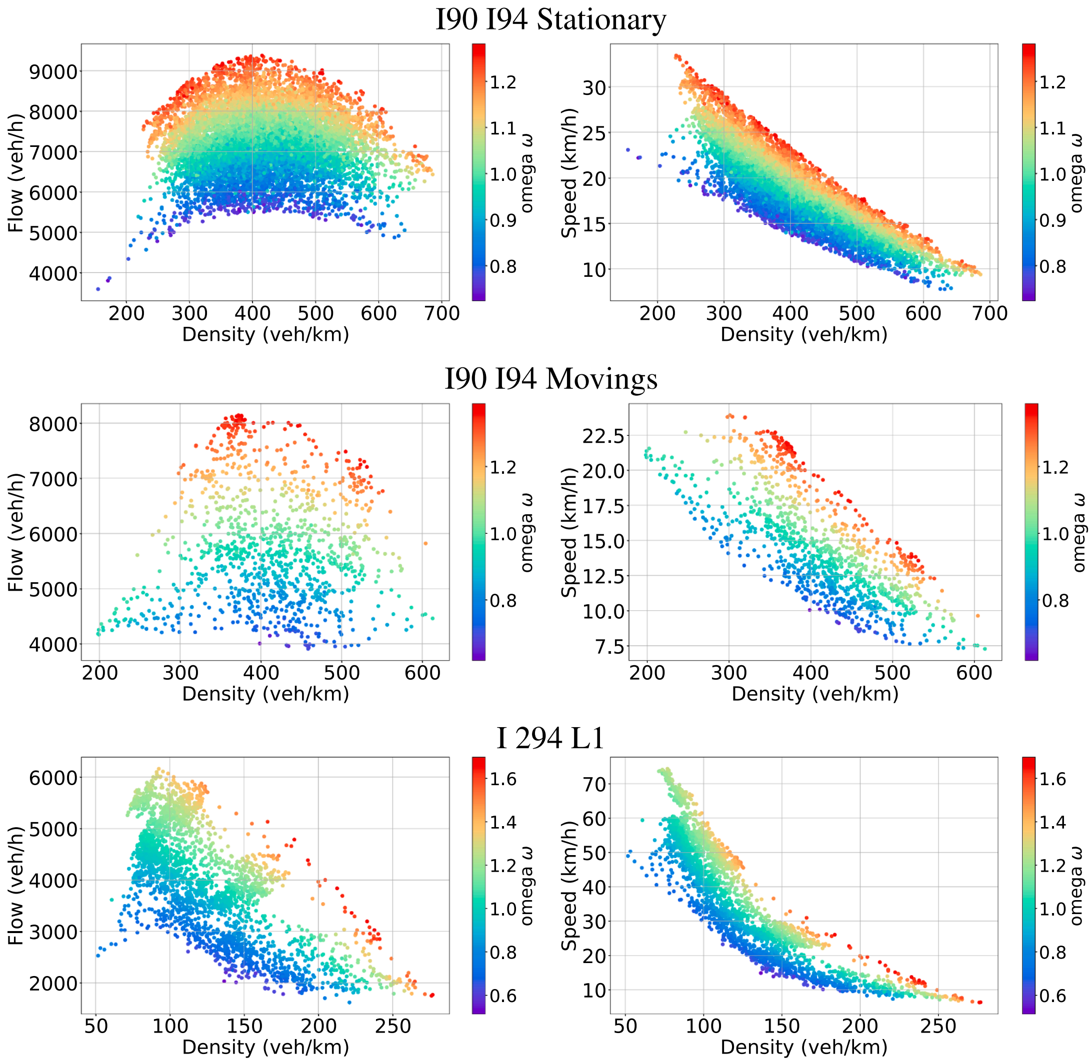

Fig. 9. The fundamental diagram separated by the learned traffic flow attribute for the TGSIM dataset.

The NN is trained with the loss function: $L(\theta_\omega) = \sum_i \left(\hat{\omega}_i(\theta_\omega) - \omega_i\right)^2$.

To get the mapping from vehicle trajectory to traffic flow attribute, we set the vehicle feature $f_{i,k}$ for vehicle k in the cell i as a seven-dimensional vector:

$$\left[\rho_i, v_k^{\text{ave}}(i), v_k^{\text{std}}(i), a_k^{\text{ave}}(i), a_k^{\text{std}}(i), C_k^{\text{absave}}(i), C_k^{\text{std}}(i)\right] \in \mathbb{R}^7, \tag{25}$$

where ρ_i is the cell density, $v_k^{\text{ave}}(i)$ and $v_k^{\text{std}}(i)$ are the average value and standard deviation of its speed profile in the cell, $a_k^{\text{ave}}(i)$ and $a_k^{\text{std}}(i)$ are the average value and standard deviation of its acceleration profile in the cell, $C_k^{\text{absave}}(i)$ and $C_k^{\text{std}}(i)$ are the average of the absolute value of is jerk profile and the standard deviation of its jerk profile as we have defined in Eqs. (3) and (4). For the first feature, the cell density is calculated via the Edie's formula, and it reflects the overall traffic condition within the cell. For the last six features, they are calculated directly from the vehicle trajectories within the cell, without any information about the vehicles' historical motion. We note that the last two features have been used to get driver's attribute ω^{L} in Section 2. We directly use C^{absave} and C^{std} instead of ω^{L} in this Section. This is because that in the scarce data scenario, for a new-arriving vehicle, its ω^{L} value requires historical trajectory, which is unavailable. And the C^{absave} and C^{std} values are available directly from its current trajectory. To summarize, all elements in the vehicle feature vector $f_{i,k}$ are obtained only using vehicle trajectories within the current cell i. We use a feed-forward fully connected neural network with 7 hidden layers and 50 neurons in each hidden layer. The output of the NN is the one-dimensional vehicle trajectory feature. We note that after the training is finished, the traffic flow attribute is reconstructed via forward calculation using the learned NN, which has a low computation cost.

In Fig. 9, we give the scatter plot of $\rho - v$ and $\rho - q$ separated by the learned $\hat{\omega}$ value on the TGSIM dataset. We see that the proposed method presents a clear separation for the fundamental diagram. We also test the proposed method using the NGSIM dataset,

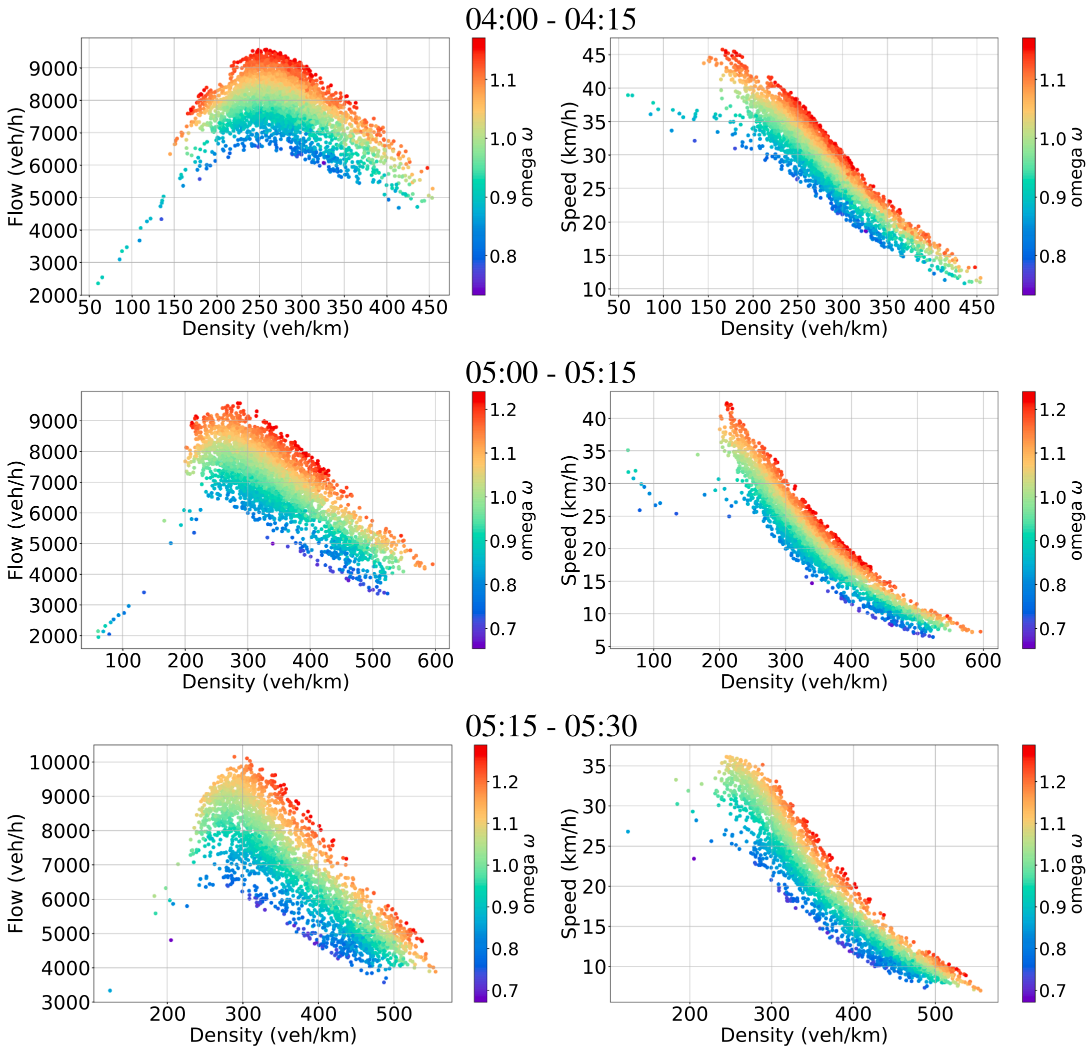

Fig. 10. The fundamental diagram separated by the learned traffic flow attribute for the NGSIM dataset.

Table 2
The calibration error (%) for one-variable fundamental diagram and two-variable fundamental diagram.

	NGSIM			TGSIM		
	04:00-04:15	05:00-05:15	05:15-05:30	I90-I94 Stationary	I90-I94 Movings	I-294
$V(\rho)$	8.50	11.16	12.19	11.10	18.21	21.74
$\mathcal{V}(\rho,\omega)$	1.46	1.65	1.86	2.45	2.11	2.02

and we plot the result in Fig. 10. We give the calibration error on these two datasets in Table 2. The results show that the proposed method learns an accurate mapping from microscopic vehicle features to macroscopic traffic flow attributes.

Remark 2 (Comparison of the two reconstruction methods with abundant data or scarce data). Although the reconstruction procedures differ between Sections 4 and 5, both aim to construct a unified pipeline that obtains the traffic flow attribute ω from vehicle trajectories and calibrates the two-dimensional fundamental diagram $\mathcal{V}(\rho,\omega)$ as in Fig. 1. In Section 4, we directly obtain ω value from vehicle trajectories and then fit the fundamental diagram $\mathcal{V}(\rho,\omega)$. In contrast, neither ω nor the functional form of $\mathcal{V}(\rho,\omega)$ is directly observable in Section 5. Jointly learning both from the available data is therefore ill-posed, as it admits infinitely many solutions. For example, if $\mathcal{V}(\rho,\omega)$ is a valid solution, then any reparameterization $\tilde{\omega} = g(\omega)$ leads to an equivalent solution $\mathcal{V}(\rho, g^{-1}(\tilde{\omega}))$, where g^{-1} is the inverse mapping of g. To address this ambiguity, we assign a physical interpretation to ω based on prior analysis in Section 4, where the heterogeneity is primarily attributed to variations in the maximum speed. Accordingly, we assume a multiplicative form of the fundamental diagram as in Eq. (22) and obtain ω from observed (ρ, v) data. In both cases, the proposed heterogeneity-dependent fundamental diagram $\mathcal{V}(\rho, \omega)$ consistently captures the macroscopic traffic behavior and ensures coherence across modeling.

A notable difference between the two settings can also be observed from the resulting fundamental diagram, as shown in Fig. 9 and Fig. 6(b). In the abundant-data scenario shown in Fig. 6(b), different values of ω tend to appear in specific density regimes, i.e., the distribution of ω is not uniform over ρ. This is because ω is reconstructed from intrinsic driver attributes, and the observed pattern reflects how drivers with different characteristics operate under different traffic densities. In contrast, in the scarce-data scenario, each ω value spans the full range of densities as in Fig. 9. The definition of ω in Eq. (22) effectively normalizes speed with respect to density and removes the dependence of ω on ρ. As a result, the learned ω represents a heterogeneity factor that is largely decoupled from density, leading to a more uniform distribution across traffic states. The observed difference of fundamental diagrams in the two scenarios reflects the distinct reconstruction methods adopted in each setting: traffic heterogeneity is explicitly characterized by physically interpretable driver attributes when data is abundant, whereas it is implicitly captured through data-driven inference from limited trajectory observations in the scarce-data setting.

5.2. Mixed traffic analysis

A key advantage of the proposed reconstruction framework is its ability to reconstruct macroscopic traffic flow attributes directly from existing mixed-autonomy trajectory data, even when the data is sparse, incomplete, and unbalanced across vehicle classes. In current real-world traffic, mixed-autonomy datasets such as TGSIM contain only a small number of experimental AVs, and continuous historical trajectories for individual vehicles are generally unavailable. The proposed framework overcomes this limitation by learning a direct mapping from trajectory features within the current spatial-temporal cell to macroscopic flow attributes. In contrast to traditional macroscopic traffic flow validation approaches, which require dense Eulerian measurements over entire road segments, our method only uses locally available Lagrangian trajectories as in Eq. (12) and therefore aligns naturally with the data collection mechanisms of mixed-autonomy traffic.

In this part, we utilize the proposed method to analyze the macroscopic traffic flow attributes to show how AVs affect traffic flow. We use the TGSIM dataset, where AVs travel with HVs in real highways. In Fig. 11, we compare the distribution of driver attributes and the scatter plot of density-speed and density-flow for two datasets in TGSIM: I90-I94 Stationary and I294 L1. We neglect the I90-I94 Moving dataset for this part, since it collects traffic data around the probe AVs. Therefore, almost all data corresponds to mixed traffic. Fig. 11(a) and (d) give the distribution of driver attributes of AVs and HVs in the two datasets. Fig. 11(b) and (e) plot the density-flow scatter, where green points represent cells containing only HVs, while red points represent mixed cells containing both AVs and HVs. Comparing these two datasets, we see that in the I90-I94 Stationary dataset, AVs exhibit a narrower distribution range as in Fig. 11(a). The fundamental diagram in Fig. 11(b)(c) shows that mixed cells also exhibit a reduced scatter range, suggesting lower macroscopic heterogeneity. For the I-294 dataset, AVs and HVs exhibit approximately the same distribution range of microscopic attributes as in Fig. 11(d). Correspondingly, the fundamental diagram in Fig. 11(e)(f) indicates that pure HV traffic and mixed traffic exhibit a similar scatter range. These findings suggest that heterogeneity serves as a bridge between microscopic and macroscopic traffic dynamics. Reduced heterogeneity in microscopic vehicle motion leads to reduced heterogeneity in macroscopic traffic flow. Moreover, heterogeneity does not lie only between AVs and HVs, but rather among individual vehicles.

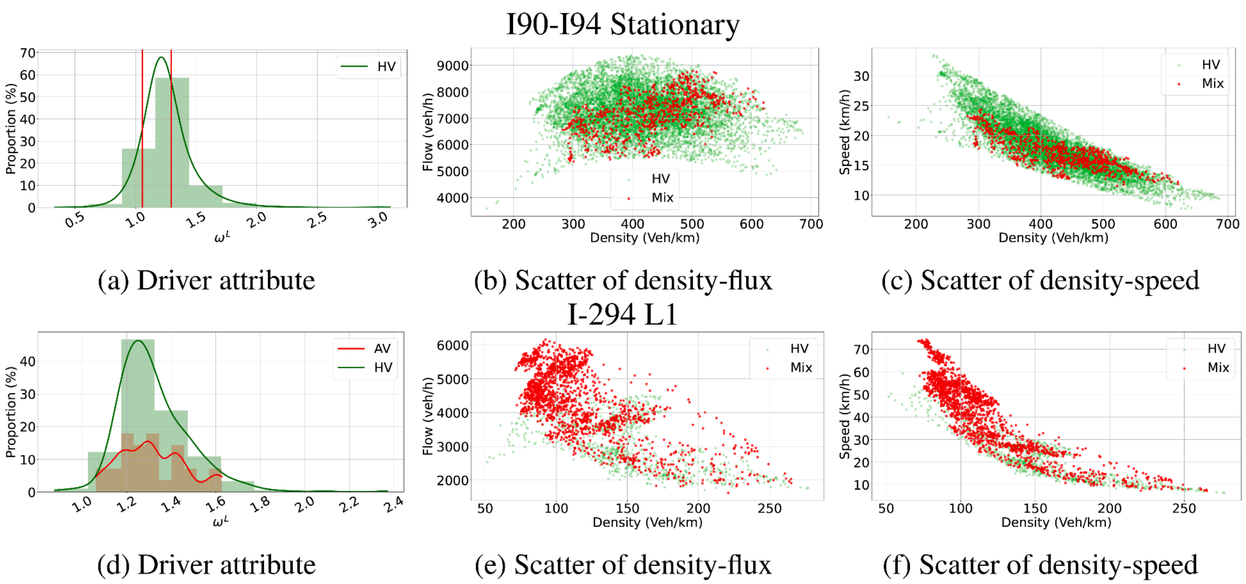

Fig. 11. The fundamental diagram of the TGSIM dataset. The green points correspond to the cells that only contain HVs, and the red points are from the traffic states for cells that contain both AVs and HVs.

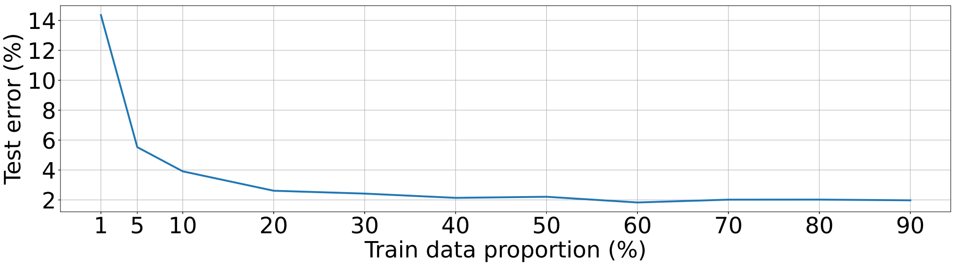

Fig. 12. The test error when using different proportion data as the training data.

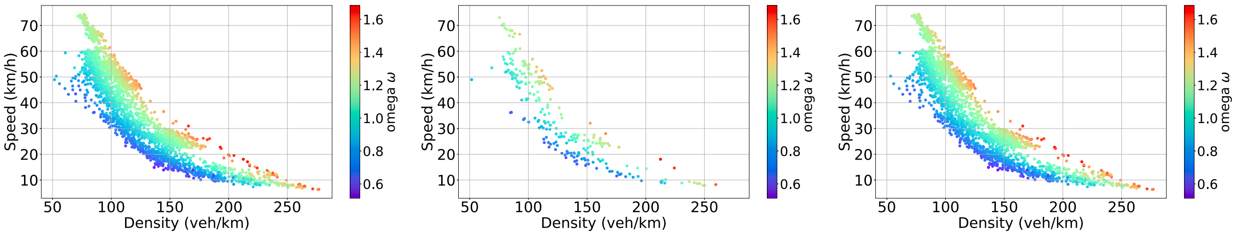

(a) All data (b) Train data (c) Test data

Fig. 13. The density-speed scatter plot when we only select 10 % as the training data.

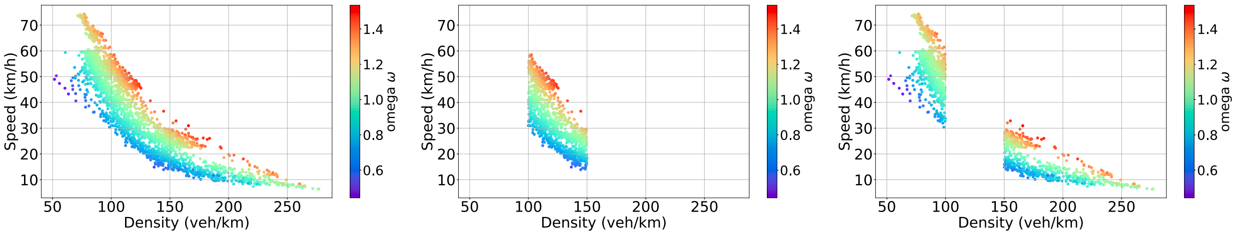

(a) All data (b) Train data (c) Test data

Fig. 14. The density-speed scatter plot when we only select these data within a given range of density as the training data.

5.3. *Sensitivity analysis*

In this part, we conduct sensitivity analysis to analyze the performance of the designed reconstruction method under varying conditions.

5.3.1. *The effect of training data*

In the previous simulation, we randomly select 80 % data from all cells as the training data and other 20 % data is used as the test data. In Fig. 12, we vary the proportion of training data from 1 % to 90 % and plot the calibration error evaluated on the test data. The single FD gives a calibration error around 20 %. We see that with a scarce data, the proposed reconstruction method still present a calibration error lower than 14 %. In Fig. 13, we give the scatter plot when we only use 10 % data as the training dataset. The low calibration error and clear separation in the fundamental diagram demonstrate that the proposed algorithm can effectively learn a micro-to-macro mapping even with scarce trajectory data.

We also test the generalization ability of the proposed method on different traffic conditions. We generate the training data from these cells whose density is within the given range of 100 veh/km to 150 veh/km. And other cells are used as test data. Fig. 14 gives the scatter fundamental diagram on both the training data and test data. The calibration error on the test data is 2.65 %. We see that the proposed method can generalize to unseen both more free traffic conditions (density is smaller than 100 veh/km) and more congested traffic (density is larger than 150 veh/km). We further shows the probability distribution of the calibration error under varying traffic conditions in Fig. 15. We see that when applying the proposed micro-macro mapping to unseen traffic conditions, a majority of the calibration error is smaller than 20 %, which is approximately the calibration error when using a single FD. For example, when the free traffic with density smaller than 100 veh/km (blue color in Fig. 15), we see that nearly 90 % of the calibration error is less than 10 %. For the congested traffic given in orange color corresponding to density between 150 veh/km to 200 veh/km, a majority of the calibration error is also lower than 10 %. We also note that, as the difference between the training data and test

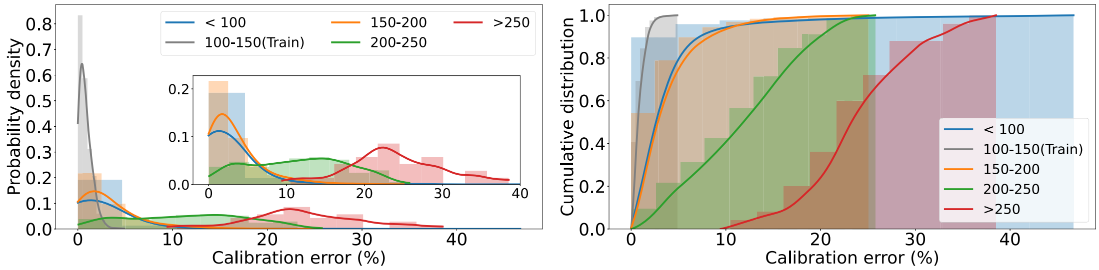

(a) Probability density (b) Cumulative distribution

Fig. 15. Distribution of the fundamental diagram calibration error under varying traffic conditions. The legend gives the range of traffic density (in veh/km). We use traffic data whose density is within 100 veh/km to 150 veh/km as the training data. More free traffic (density smaller than 100 veh/km) and more congested traffic (density higher than 150 km/h) are used as the test data.

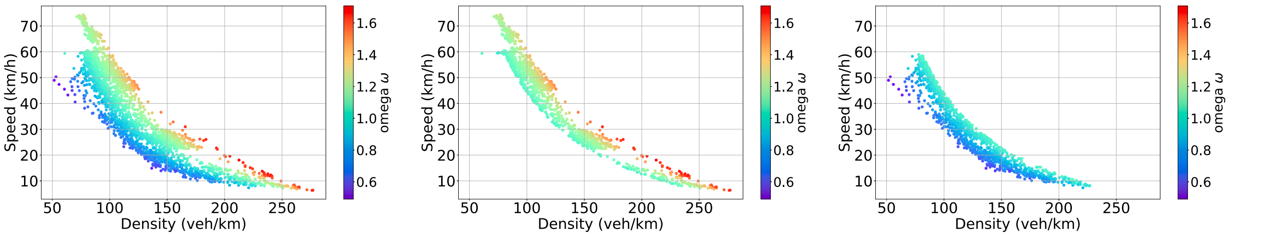

(a) All data (b) Train data (c) Test data

Fig. 16. The density-speed scatter plot when we only select these data with $\omega > 1$ as the training data.

Table 3
Calibration error on the test data (%).

Name	Error	Name	Error
\	\	MACRO	13.59
MICRO-v	14.52	MACRO-v	1.93
MICRO-j	14.99	MACRO-j	9.96
MICRO-a	15.09	MACRO-a	11.17
MICRO	10.79	ALL	2.02

data increases, the test error also increases. For example, when the test density is higher than 200 veh/km, the calibration error has a wider range of distribution, but still with a majority smaller than 20 %. These results indicate that the proposed method can also build an accurate micro-macro mapping with unseen traffic conditions.

In Fig. 16, we generate the training dataset by only keeping these cells whose ω value is greater than one. And those cells with $\omega < 1$ are taken as the test data. The calibration error on the test data is 2.84 %. Fig. 16 gives the result on the training and test data. We see that there is also a clear separation on the test data. Therefore, when there are more aggressive drivers, the proposed reconstruction method still brings an accurate mapping from microscopic trajectories to macroscopic attributes.

5.3.2. *The effect of vehicle features*

In previous simulation, the vehicle feature include mainly four parts: traffic density, vehicle speed, vehicle acceleration, and vehicle jerk. In this part, we analyze how the choice of vehicle features affect the calibration error. We consider three types of variants:

- MACRO: we only use traffic density as the feature, and the feature is a thus a scalar value.
- We only use those features from the single vehicle trajectory.
  - MICRO-v: we only use the average and standard deviation of the vehicle's speed profile.
  - MICRO-a: we only use the average and standard deviation of the vehicle's acceleration profile.
  - MICRO-j: we only use the average, average of absolute, and standard deviation of the vehicle's speed profile.
- Mixed with both macro density and micro values:
  - MACRO-v: we use the cell density, average of the vehicle's speed, and the standard deviation of its speed.
  - MACRO-a: we use the cell density, average of the vehicle's acceleration, and the standard deviation of its acceleration.
  - MACRO-j: we use the cell density, average of the vehicle's jerk, average of the absolute values of its jerk, and the standard deviation of its jerk.

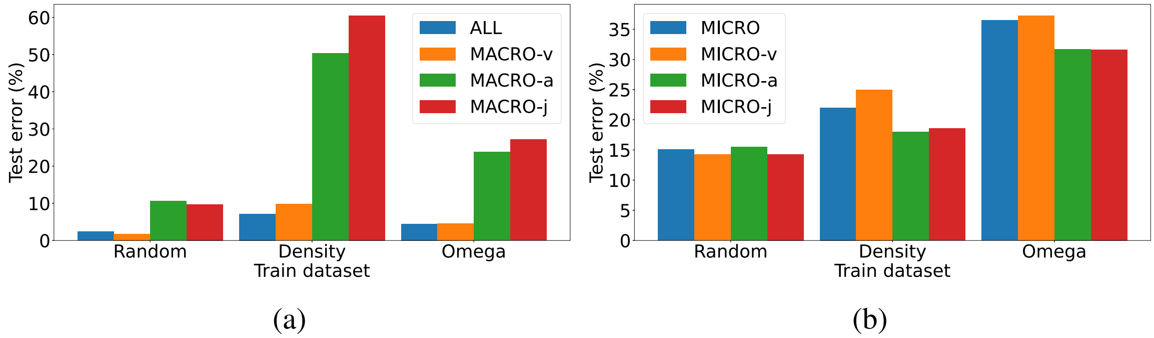

Fig. 17. The fundamental diagram calibration error under different training datasets and different choices of features that used to map to the macroscopic traffic flow attribute.

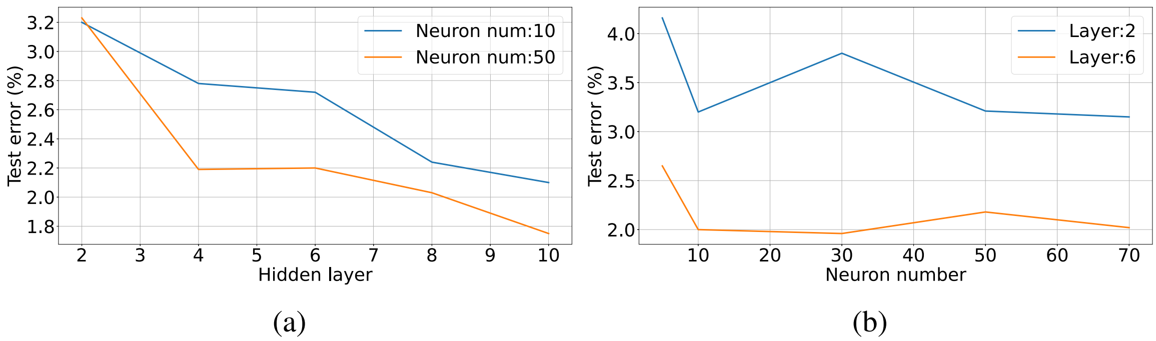

Fig. 18. The fundamental diagram calibration error with different NN size. We see that the proposed method has a low calibration error even with a simple neural network structure.

– ALL: we use all features, i.e., the feature is a eight-dimension vector.

We randomly select 80 % data as the training data and report in Table 3 the calibration error on the test data for different variants of the proposed method. In each row, we use the same trajectory feature and compare the calibration error for micro-only vs micro + macro. As the result show, incorporating surrounding traffic information (i.e., cell density) greatly reduces the test error. For example, in the second row, when we only use speed average and speed standard deviation as vehicle features, i.e., MICRO-v, the calibration error is around 15 %. But when we also incorporate traffic density into the vehicle feature, the calibration error reduces to around 2 %. Comparing the errors for the first column, we see that the MICRO, which incorporates features from speed, acceleration, and jerk, gives the lowest calibration error. Comparing results in the third column, we see the MACRO-v, which use three features of density, speed average, speed standard deviation, and the ALL, which uses density and all features from speed, acceleration, and jerk, give the lowest calibration error. The comparison of calibration error implies that the speed information is the main features when we map from microscopic trajectories to macroscopic flow attributes.

In Fig. 17, we further compare the test error by different variants on different training datasets. We consider three training datasets: ‘Random’ where 30 % of data is randomly selected as the training data, ‘Density’ where cells whose density is within 100 veh/km to 150 veh/km are the training data, and ‘Omega’ where cells with $\omega > 1$ are selected as training data. We see that in the Random case, the MICRO-v has a slight improvement over ALL. But for the Density and Omega case, where the test data contains unseen traffic conditions, the ALL version gives a lower calibration error than MICRO-v. Therefore, ALL that contains traffic density information has a better generalization ability.

5.3.3. The effect of the NN size

We run simulations with varying numbers of hidden layers and neurons to analyze how the proposed micro-macro mapping method works under different NN sizes. We give the test error in Fig. 18. In Fig. 18(a), we fix the neuron numbers in each hidden layers and run simulations when the number of hidden layers changes. In Fig. 18(b), we fix the number of hidden layers and change the neuron numbers in each hidden layer. Increasing the hidden layers or the number of neurons brings a lower error, which agrees with naive intuition. We also note that even using a very small network with only 2 hidden layers and 5 neurons in each hidden layer, we still have an accurate calibration with the calibration error lower around 4 %. With such a straightforward and easy-to-implement neural network structure, the training computation cost is very low, and the proposed method can be easily applied to practical traffic systems.

6. Conclusion

In this paper, we utilize heterogeneity in mixed-autonomy traffic and bridge the gap between Lagrangian trajectory data and Eulerian traffic flow models. We demonstrate that heterogeneity exists not only between AVs and HVs but also within each class individually. And the heterogeneity between individual vehicles, regardless of AVs or HVs, can exceed the average inter-class heterogeneity, which motivates the use of a continuous-valued traffic-heterogeneity flow attribute over discrete multi-class models. Based on real trajectory data, we design a micro-to-macro mapping that incorporates drivers' attributes and local behavioral features to reconstruct flow attributes. The mapping provides insight into how AV controllers influence mixed traffic flow and offers a macroscopic formulation that can integrate AV-collected data. We also extend our approach to address the more challenging scenario of scarce data availability by designing a data-driven reconstruction mapping. Analysis using real trajectory data validates the effectiveness of the proposed mapping in capturing microscopic-macroscopic relations. We also show that the model exhibits strong generalization capability when applied to unseen traffic conditions.

This work provides several promising directions for future research. First, while we adopt a fully connected neural network in this study, exploring more advanced architectures such as graph-based or attention-based networks, may improve the interpretability of the mapping. Second, alternative methods for extracting driver attributes from trajectory data can be investigated. In this work, features are computed using statistical measures (e.g., average and standard deviation) over the full trajectory, which requires complete driving records. Incorporating other features could enhance robustness against data noise or temporary data unavailability caused by communication failure. Third, while wave propagation prediction is an important application of macroscopic traffic flow models, we only validate the flow pattern prediction in Section 4 on heterogeneous HV dataset. The traffic-wave propagation of mixed traffic dynamics have not been covered in this paper, since the mixed-autonomy TGSIM dataset provides trajectory data only for localized roadway segments, lacking the full spatiotemporal coverage required for such validation. We instead validate our model through the fundamental diagram in Section 5. Using the proposed attribute-based model to capture wave propagation of mixed traffic will be of future interest when large-scale spatiotemporal datasets become available.

CRediT authorship contribution statement

Chenguang Zhao: Writing – original draft, Visualization, Validation, Investigation, Data curation; **Huan Yu:** Writing – review & editing, Writing – original draft, Supervision, Methodology, Funding acquisition, Formal analysis, Conceptualization.

Acknowledgement

This work was supported by the National Natural Science Foundation of China No.12526214, and No.62203131.

Data availability

Data will be made available on request.

Appendix A. Data collection and features of the datasets

The Ring dataset was collected in Beijing, China (Zheng et al., 2021). The authors conducted an experiment on an 800-meter ring road and collected the trajectories of 40 participating human drivers over a period of approximately 20 min. The measurement errors for position and speed were 1 m and 1 km/h, respectively. The sampling rate was 10 Hz.

The CATS dataset was collected by Shi and Li (2021) using a Lincoln MKZ autonomous vehicle. The AV traveled on SR-56 in Florida, USA. The data was collected at a sampling rate of 1 Hz, with a position accuracy of 0.26 m and a speed accuracy of 0.089 m/s. The OpenACC dataset (Makridis et al., 2021) was collected by the European Commission's Joint Research Center across Hungary, Italy, and Sweden. Various commercial ACC vehicles were used to collect the data, including the Tesla Model 3, BMW X5, Toyota RAV4, and Mercedes A-Class. The sampling rate ranged from 3 Hz to 100 Hz. The position accuracy ranged from approximately 0.02 m to 0.5 m, and the speed accuracy was around 1 km/h. The CentralOhio dataset was collected in Ohio, USA (Xia et al., 2023; Seitz et al., 2024). The measurement errors for position and speed were approximately 1 m and 0.1 m/s, respectively.

The distributions of vehicle speed and gap in the datasets are shown in Fig. A.1. The results indicate that the collected data span a wide range of traffic scenarios. The speed profiles include complete stops (i.e., zero speed), as seen in CATS Fig. A.1(c) and CentralOhio Fig. A.1(d). They also capture free-flow conditions with high speeds around 30 m/s, as in OpenACC Fig. A.1(b). The wide range in the gap distributions further demonstrates that the datasets cover diverse traffic conditions.

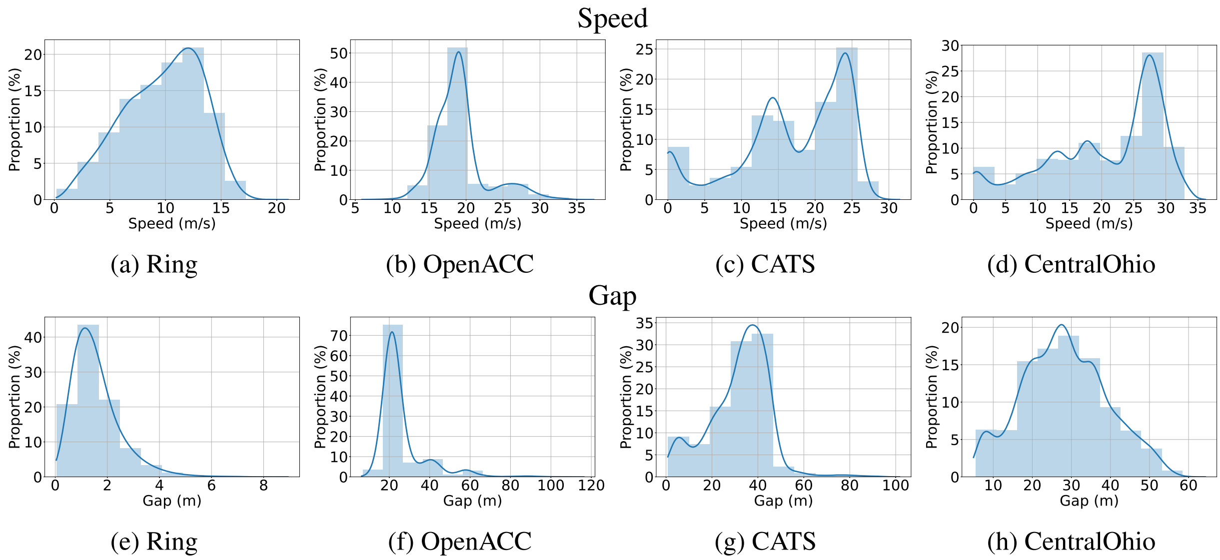

Fig. A.1. Speed and gap distribution in datasets.

Appendix B. Car-following model calibration

We run generic algorithms to calibrate the OVM car-following model Eq. (1). For a vehicle i, the objective function is to minimize the calibration error for the gap and speed:

$$\sum_j \left(\hat{s}_i(t_j) - s_i(t_j)\right)^2 + \alpha\left(\hat{v}_i(t_j) - v_i(t_j)\right)^2, \tag{B.1}$$

where j denotes the time step, and $\alpha = (s_i^*/v_i^*)^2$ is the coefficient with s_i^* and v_i^* being the average gap and speed of the trajectory. We set the range for the OVM parameters as: $\tau \in [0, 20]$, $\beta \in [0, 5]$, $s^0 \in [1, 20]$, $T \in [0, 5]$, $V^{\mathrm{f}} \in [0, 50]$. We run the generic algorithm for 500 iterations. We evaluate the calibration accuracy via:

$$E_s = \frac{\sum_j (\hat{s}(t_j) - s(t_j))^2}{\sum_j (s(t_j))^2} \times 100\,\%, \quad E_v = \frac{\sum_j (\hat{v}(t_j) - v(t_j))^2}{\sum_j (v(t_j))^2} \times 100\,\%. \tag{B.2}$$

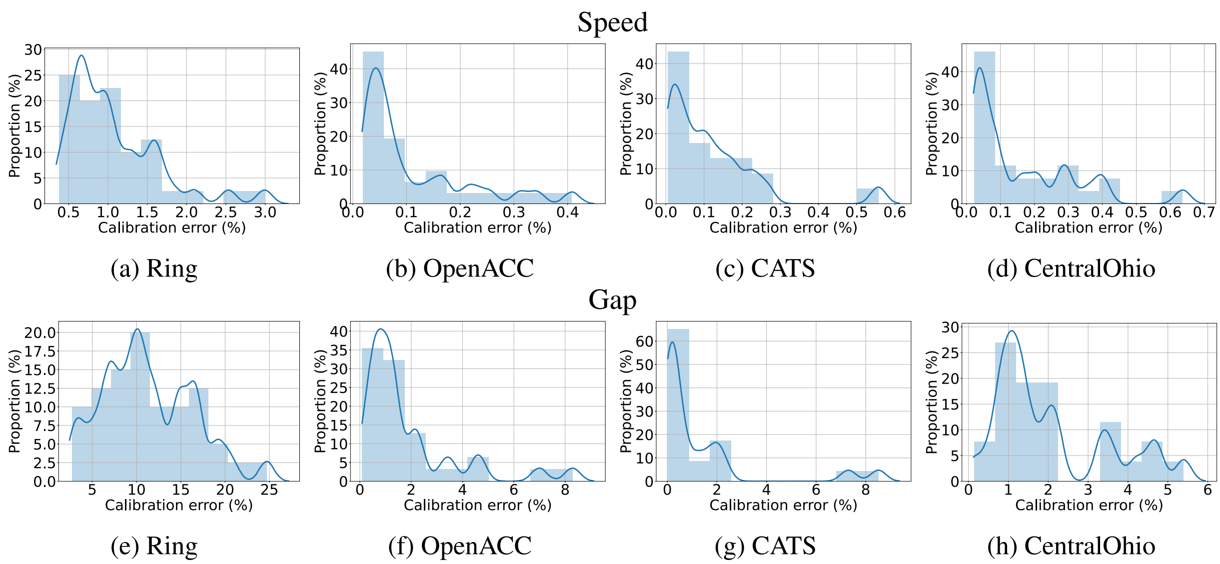

Fig. B.2. Calibration error of the OVM.

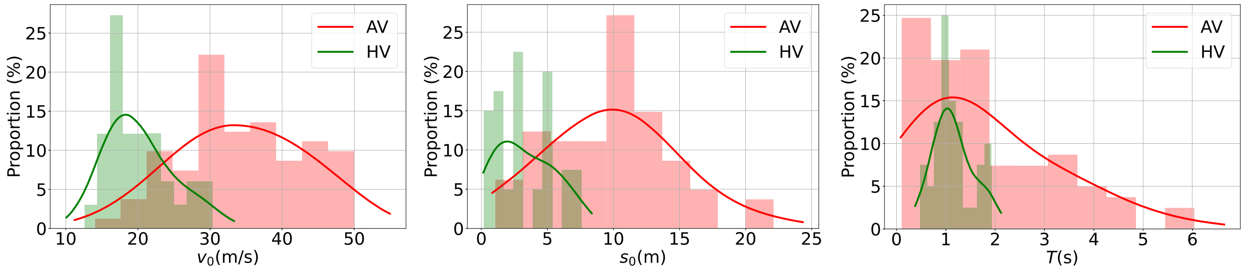

(a) (b) (c)

Fig. B.3. Distribution of calibrated IDM car-following model parameters for HV and AV.

We choose not to use the RMSE as $\left(\frac{\hat{v}(t_j)-v(t_j))^2}{v(t_j)}\right)^2$ since the vehicle is at stop, i.e., $v(t)=0$, during some time periods. We present the calibration error in the four datasets in Fig. B.2. The results show that for the three AV datasets, the calibrated OVM accurately describes car-following dynamics, with the gap error less than 10 % and the speed error less than 1 %. For the HV Ring dataset, the calibration error is higher, as human drivers exhibit more uncertain driving behaviors that are difficult to formulate accurately. Nevertheless, the OVM model still provides an accurate representation of the trajectory. For the gap, the majority of the error is lower than 10 %. And for speed, the error is around 1 %.

We also calibrate the IDM model and give the calibrated free-speed v_0, time gap T, minimum spacing s_0 in Fig. B.3. Similar to the results in Fig. 2 with OVM, there exists heterogeneity not only in the AV-class and HV-class, but also within both classes.

References

Alan, A., He, C.R., Molnar, T.G., Mathew, J.C., Bell, A.H., Orosz, G., 2024. Integrating safety with performance in connected automated truck control: experimental validation. IEEE Trans. Intell. Veh. 9 (1), 3075–3088.
Ameli, M., Mcquade, S.T., Lee, J.W., Bunting, M., Nice, M.W., Wang, H., Barbour, W., Weightman, R., Denaro, C., Delorenzo, R., et al., 2025. Design, preparation, and execution of the 100-AV field test for the CIRCLES consortium: methodology and implementation of the largest mobile traffic control experiment to date. IEEE Control Syst. 45 (1), 139–155.
Ammourah, R., Beigi, P., Fan, B., Hamdar, S.H., Hourdos, J., Hsiao, C.-C., James, R., Khajeh-Hosseini, M., Mahmassani, H.S., Monzer, D., et al., 2025. Introduction to the third generation simulation dataset: data collection and trajectory extraction. Transp. Res. Rec. 2679 (1), 1768–1784.
Aw, A., Rascle, M., 2000. Resurrection of "second order" models of traffic flow. SIAM J. Appl. Math. 60 (3), 916–938.
Barth, M., 2024. Co-benefits and tradeoffs between safety, mobility, and environmental impacts for connected and automated vehicles. IEEE Trans. Intell. Transp. Syst. 25 (4), 184–213.
Batkovic, I., Gupta, A., Zanon, M., Falcone, P., 2023. Experimental validation of safe MPC for autonomous driving in uncertain environments. IEEE Trans. Control Syst. Technol. 31 (5), 2027–2042.
Beigi, P., Hamdar, S., Talebpour, A., Mahmassani, H., 2025. Impact of heavy vehicles on headway distributions: study using naturalistic urban expressway trajectories. Transp. Res. Rec. , 03611981251324198.
Chiarello, F.A., Friedrich, J., Goatin, P., Gottlich, S., 2020. Micro-macro limit of a nonlocal generalized aw-rascle type model. SIAM J. Appl. Math. 80 (4), 1841–1861.
Chiarello, F.A., Piccoli, B., Tosin, A., 2021. A statistical mechanics approach to macroscopic limits of car-following traffic dynamics. Int. J. Non-Linear Mech. 137, 103806.
Choe, T., Skabardonis, A., Varaiya, P., 2002. Freeway performance measurement system: operational analysis tool. Transp. Res. Rec. 1811 (1), 67–75.
Dimarco, G., Tosin, A., Zanella, M., 2022. Kinetic derivation of aw-Rascle-Zhang-type traffic models with driver-assist vehicles. J. Stat. Phys. 186 (1), 17.
Ercan, T., Onat, N.C., Keya, N., Tatari, O., Eluru, N., Kucukvar, M., 2022. Autonomous electric vehicles can reduce carbon emissions and air pollution in cities. Transp. Res. D Transp. Environ. 112, 103472.
Fan, S., Herty, M., Seibold, B., 2014. Comparative model accuracy of a data-fitted generalized aw-Rascle-Zhang model. Netw. Heterog. Media 9 (2), 239–268.
FHWA, 2007. Next generation simulation (NGSIM). https://ops.fhwa.dot.gov/trafficanalysistools/ngsim.htm.
Gloudemans, D., Wang, Y., Ji, J., Zachar, G., Barbour, W., Hall, E., Cebelak, M., Smith, L., Work, D.B., 2023. I-24 MOTION: an instrument for freeway traffic science. Transp. Res. C Emerg. Technol. 155, 104311.
Gunter, G., Gloudemans, D., Stern, R.E., McQuade, S., Bhadani, R., Bunting, M., Delle Monache, M.L., Lysecky, R., Seibold, B., Sprinkle, J., et al., 2020. Are commercially implemented adaptive cruise control systems string stable? IEEE Trans. Intell. Transp. Syst. 22 (11), 6992–7003.
Gunter, G., Janssen, C., Barbour, W., Stern, R.E., Work, D.B., 2019. Model-based string stability of adaptive cruise control systems using field data. IEEE Trans. Intell. Veh. 5 (1), 90–99.
Hayat, A., Alanqary, A., Bhadani, R., Denaro, C., Weightman, R.J., Xiang, S., Lee, J.W., Bunting, M., Gollakota, A., Nice, M.W., et al., 2025. Traffic smoothing using explicit local controllers: experimental evidence for dissipating stop-and-go waves with a single automated vehicle in dense traffic. IEEE Control Syst. 45 (1), 95–110.
Holden, H., Risebro, N.H., 2024. The continuum limit of non-local follow-the-leader models. ESAIM: Math. Model. Numer. Anal. 58 (4), 1523–1539.
Hu, X., Zheng, Z., Chen, D., Sun, J., 2023. Autonomous vehicle's impact on traffic: empirical evidence from Waymo open dataset and implications from modelling. IEEE Trans. Intell. Transp. Syst. 24 (6), 6711–6724.
Hu, X., Zheng, Z., Chen, D., Zhang, X., Sun, J., 2022. Processing, assessing, and enhancing the Waymo autonomous vehicle open dataset for driving behavior research. Transp. Res. C Emerg. Technol. 134, 103490.
Huang, K., Di, X., Du, Q., Chen, X., 2020. A game-theoretic framework for autonomous vehicles velocity control: bridging microscopic differential games and macroscopic mean field games. Discrete Contin. Dyn. Syst.-B 25 (12), 4869–4903.
Huang, L., Qin, J., Zhou, Y., Zhu, F., Liu, L., Shao, L., 2023. Normalization techniques in training dnns: methodology, analysis and application. IEEE Trans. Pattern Anal. Mach. Intell. 45 (8), 10173–10196.
Hui, S., Zhang, M., 2024. An anisotropic traffic flow model with look-ahead effect for mixed autonomy traffic. Transp. Res. Rec. 2680 (5), 320-331.
Imran, W., Tettamanti, T., Varga, B., Bifulco, G.N., Pariota, L., 2024. Macroscopic modeling of connected, autonomous and human-driven vehicles: a pragmatic perspective. Transp. Res. Interdiscip. Perspect. 24, 101058.

Jiang, J., Zhou, Y., Wang, X., Ahn, S., 2024. On dynamic fundamental diagrams: implications for automated vehicles. Transp. Res. B Methodol. 189, 102979.
Jin, I.G., Avedisov, S.S., He, C.R., Qin, W.B., Sadeghpour, M., Orosz, G., 2018. Experimental validation of connected automated vehicle design among human-driven vehicles. Transp. Res. C Emerg. Technol. 91, 335–352.
Lebacque, J.-P., Mammar, S., Haj-Salem, H., 2007. Generic second order traffic flow modelling. Transp. Traffic Theory 2007, 755–776.
Lee, J.W., Wang, H., Jang, K., Lichtlé, N., Hayat, A., Bunting, M., Alanqary, A., Barbour, W., Fu, Z., Gong, X., et al., 2025. Traffic control via connected and automated vehicles (CAVs): an open-road field experiment with 100 CAVs. IEEE Control Syst. 45 (1), 28–60.
Levin, M.W., Boyles, S.D., 2016. A multiclass cell transmission model for shared human and autonomous vehicle roads. Transp. Res. C Emerg. Technol. 62, 103–116.
Li, J., Chen, D., Zhang, M., 2022. Equilibrium modeling of mixed autonomy traffic flow based on game theory. Transp. Res. B Methodol. 166, 110–127.
Li, P., Parker, S.T., Noyce, D.A., 2024. Automated vehicles vs. human drivers: modeling driving behavior using data from field experiments. In: International Conference on Transportation and Development 2024, pp. 560–572.
Li, S., Zheng, H., Wang, J., Chen, C., Xu, Q., Wang, J., Li, K., 2025. Influence of information flow topology and maximum platoon size on mixed traffic stability. Transp. Res. C Emerg. Technol. 171, 104950.
Li, T., Chen, D., Zhou, H., Laval, J., Xie, Y., 2021. Car-following behavior characteristics of adaptive cruise control vehicles based on empirical experiments. Transp. Res. Part B Methodol. 147, 67–91.
Li, X., 2022. Trade-off between safety, mobility and stability in automated vehicle following control: an analytical method. Transp. Res. B Methodol. 166, 1–18.
Liu, M., Yurtsever, E., Fossaert, J., Zhou, X., Zimmer, W., Cui, Y., Zagar, B.L., Knoll, A.C., 2024. A survey on autonomous driving datasets: statistics, annotation quality, and a future outlook. IEEE Trans. Intell. Veh. 9 (11), 7138–7164.
Logghe, S., Immers, L.H., 2008. Multi-class kinematic wave theory of traffic flow. Transp. Res. B Methodol. 42 (6), 523–541.
Makridis, M., Mattas, K., Anesiadou, A., Ciuffo, B., 2021. OpenACC. an open database of car-following experiments to study the properties of commercial ACC systems. Transp. Res. C Emerg. Technol. 125, 103047.
Makridis, M., Mattas, K., Ciuffo, B., Re, F., Kriston, A., Minarini, F., Rognelund, G., 2020. Empirical study on the properties of adaptive cruise control systems and their impact on traffic flow and string stability. Transp. Res. Rec. 2674 (4), 471-484.
Mao, P., Ji, X., Li, S., Qu, X., Ran, B., 2024. An internal stochastic car-following model: stochasticity analysis of mixed traffic environment. Phys. A Stat. Mech. Appl. 653, 130051.
Martínez, I., Jin, W.-l., 2020. Stochastic LWR model with heterogeneous vehicles: theory and application for autonomous vehicles. Transp. Res. Procedia 47, 155–162.
Masello, L., Sheehan, B., Murphy, F., Castignani, G., McDonnell, K., Ryan, C., 2022. From traditional to autonomous vehicles: a systematic review of data availability. Transp. Res. Rec. 2676 (4), 161–193.
Mo, Z., Chen, X., Di, X., Iacomini, E., Segala, C., Herty, M., Lauriere, M., 2024. A game-theoretic framework for generic second-order traffic flow models using mean field games and adversarial inverse reinforcement learning. Transp. Sci. 58 (6), 1403-1426.
Ngoduy, D., Liu, R., 2007. Multiclass first-order simulation model to explain non-linear traffic phenomena. Phys. A Stat. Mech. Appl. 385 (2), 667–682.
Qian, Z.S., Li, J., Li, X., Zhang, M., Wang, H., 2017. Modeling heterogeneous traffic flow: a pragmatic approach. Transp. Res. B Methodol. 99, 183–204.
Qin, Y., Wang, H., Ni, D., 2021. Lighthill-whitham-richards model for traffic flow mixed with cooperative adaptive cruise control vehicles. Transp. Sci. 55 (4), 883–907.
Seitz, T., Karanjkar, S., Ma, J., Xia, X., James, R.M., et al., 2024. Advanced Driver Assistance System-Equipped Vehicle Datasets Collected in Central Ohio. Technical Report. United States. Federal Highway Administration. Office of Safety and ·.
Shi, H., Chen, D., Zheng, N., Wang, X., Zhou, Y., Ran, B., 2023. A deep reinforcement learning based distributed control strategy for connected automated vehicles in mixed traffic platoon. Transp. Res. C Emerg. Technol. 148, 104019.
Shi, X., Li, X., 2021. Empirical study on car-following characteristics of commercial automated vehicles with different headway settings. Transp. Res. C Emerg. Technol. 128, 103134.
Stern, R.E., Cui, S., Delle Monache, M.L., Bhadani, R., Bunting, M., Churchill, M., Hamilton, N., Pohlmann, H., Wu, F., Piccoli, B., et al., 2018. Dissipation of stop-and-go waves via control of autonomous vehicles: field experiments. Transp. Res. C Emerg. Technol. 89, 205–221.
Sun, C., Guanetti, J., Borrelli, F., Moura, S.J., 2020a. Optimal eco-driving control of connected and autonomous vehicles through signalized intersections. IEEE Internet Things J. 7 (5), 3759–3773.
Sun, P., Kretzschmar, H., Dotiwalla, X., Chouard, A., Patnaik, V., Tsui, P., Guo, J., Zhou, Y., Chai, Y., Caine, B., et al., 2020b. Scalability in perception for autonomous driving: waymo open dataset. In: Proceedings of the IEEE/CVF Conference on Computer Vision and Pattern Recognition, pp. 2446–2454.
Talebpour, A., Mahmassani, H.S., Hamdar, S.H., et al., 2024. Third generation simulation data (TGSIM): A closer look at the impacts of automated driving systems on human behavior. Technical Report. United States. Department of Transportation. Intelligent Transportation.
Tordeux, A., Costeseque, G., Herty, M., Seyfried, A., 2018. From traffic and pedestrian follow-the-leader models with reaction time to first order convection-diffusion flow models. SIAM J. Appl. Math. 78 (1), 63–79.
Vander Laan, Z., Schonfeld, P., 2020. Modeling heterogeneous traffic with cooperative adaptive cruise control vehicles: a first-order macroscopic perspective. Transp. Plan. Technol. 43 (2), 113–140.
Wang, H., Fu, Z., Lee, J.W., Zinat Matin, H.N., Alanqary, A., Urieli, D., Hornstein, S., Kreidieh, A.R., Chekroun, R., Barbour, W., Richardson, W.A., Work, D., Piccoli, B., Seibold, B., Sprinkle, J., Bayen, A.M., Delle Monache, M.L., 2025. Hierarchical speed planner for automated vehicles: a framework for lagrangian variable speed limit in mixed-autonomy traffic. IEEE Control Syst. Mag. 45 (1), 111-138.
Wang, J., Zheng, Y., Chen, C., Xu, Q., Li, K., 2021. Leading cruise control in mixed traffic flow: system modeling, controllability, and string stability. IEEE Trans. Intell. Transp. Syst. 23 (8), 12861–12876.
Wang, J., Zheng, Y., Dong, J., Chen, C., Cai, M., Li, K., Xu, Q., 2023. Implementation and experimental validation of data-driven predictive control for dissipating stop-and-go waves in mixed traffic. IEEE Internet Things J. 11 (3), 4570–4585.
Wen, X., Cui, Z., Jian, S., 2022. Characterizing car-following behaviors of human drivers when following automated vehicles using the real-world dataset. Accid. Anal. Prev. 172, 106689.
Wong, G., Wong, S.C., 2002. A multi-class traffic flow model–an extension of LWR model with heterogeneous drivers. Transp. Res. A Policy Pract. 36 (9), 827–841.
Xia, X., Meng, Z., Han, X., Li, H., Tsukiji, T., Xu, R., Zheng, Z., Ma, J., 2023. An automated driving systems data acquisition and analytics platform. Transp. Res. C Emerg. Technol. 151, 104120.
Yu, H., Yeo, H., 2025. Dynamic characteristics of commercial adaptive cruise control across driving situations: response time, string stability, and asymmetric behavior. Transp. Res. C Emerg. Technol. 170, 104931.
Zhang, H., Li, S., Li, Z., Anis, M., Lord, D., Zhou, Y., 2025. Why anticipatory sensing matters in commercial ACC systems under cut-in scenarios: a perspective from stochastic safety analysis. Accid. Anal. Prev. 218, 108064.
Zhang, H.M., 2002. A non-equilibrium traffic model devoid of gas-like behavior. Transp. Res. B: Methodol. 36 (3), 275–290.
Zhang, P., Wong, S.C., Dai, S.Q., 2009. A conserved higher-order anisotropic traffic flow model: description of equilibrium and non-equilibrium flows. Transp. Res. B Methodol. 43 (5), 562–574.
Zhang, Y., Yu, H., Auriol, J., Pereira, M., 2024. Mean-square exponential stabilization of mixed-autonomy traffic PDE system. Automatica 170, 111859.
Zhao, C., Molnar, T.G., Yu, H., 2024. Leveraging cooperative connected automated vehicles for mixed traffic safety. Transp. Res. B: Methodol. 203, 103352.
Zhao, C., Yu, H., 2024. Observer-informed deep learning for traffic state estimation with boundary sensing. IEEE Trans. Intell. Transp. Syst. 25 (2), 1602–1611.
Zhao, C., Yu, H., Molnar, T.G., 2023. Safety-critical traffic control by connected automated vehicles. Transp. Res. Part C Emerg. Technol. 154, 104230.
Zheng, S.-T., Jiang, R., Tian, J.-F., Zhang, H.M., Li, Z.-H., Gao, L.-D., Jia, B., 2021. Experimental study on properties of lightly congested flow. Transp. Res. B Methodol. 149, 1–19.
Zhou, H., Ma, K., Liang, S., Li, X., Qu, X., 2024. A unified longitudinal trajectory dataset for automated vehicle. Sci. Data 11 (1), 1123.
Zhou, H., Zhou, A., Li, T., Chen, D., Peeta, S., Laval, J., 2022. Significance of low-level control to string stability under adaptive cruise control: algorithms, theory and experiments. Transp. Res. C Emerg. Technol. 140, 103697.